Master Computer Science

3D preoperative to intraoperative registration of lymph node locations in robotic prostate cancer surgery

Name:	Hendrik Marijn Houwing
Student ID:	s2688743
Date:	dd/10/2022

Specialisation: Bioinformatics

1st supervisor: Prof.dr.ir. F.J. Verbeek

2nd supervisor: Prof.dr. F.W.B. van Leeuwen

Master's Thesis in Computer Science

Abstract

Rationale: A procedure that fits in the minimal invasive surgery methodology in prostate cancer, is the Sentinel Node (SN) procedure. This procedure tries to minimise the number of removed LNs, as research has shown that removing more LN results in higher patient complication rates. However, the complexity of the procedure makes standardisation and validation of the SN procedure a difficult task. Currently, no verifiable method in routine patient care exists that can match the SN locations in preoperative imaging with intraoperative removed SN locations. The aim of this thesis is to set a first step towards linking preoperative scans and the intraoperative SN locations. **Methods:** This thesis proposes a new method that uses video-based stereoscopic probe tracking and IMU sensor endoscope tracking to record SN locations during surgery and matches the preoperative and intraoperative volume postoperatively using a registration algorithm. The validation of this method is done in a phantom model setting, and by simulation of the registration algorithms using 13 clinical patient SPECT/CT scans. **Results:** Video-based stereo tracking resulted in a robust probe tracking solution and achieved an accuracy of 4.0±2.7mm accuracy. Combining the probe tracking with the IMU sensor data, the pattern of intraoperative SNs can be recorded, such that the registration algorithms was able to link the preoperative SN locations to the intraoperative SN locations. Chamfer matching showed that even with an error of 15±3.1mm on the intraoperative LN locations, the registration of the two volumes resulted in a correct pairing of the SNs in 81% of the cases. Errors below 15.8±3.1mm resulted in 100% of the cases in correct pairing of the SNs using chamfer matching. **Conclusion:** The registration algorithms showed to be robust, such that using the patterns of the LN, the preoperative and intraoperative volume could be registered which allowed to pair the preoperative and the corresponding intraoperative SN locations. The proposed method provides a step towards linking preoperative imaging to intraoperative SN locations in clinic.

Table of contents

Chapter 1
Introduction

In Prostate cancer, new techniques have been introduced lowering patient complications (robotic surgery [1]) or improving efficiency of the identification of lymph nodes (LN) (DROP-IN gamma probe [2]). Another example of such techniques is the Sentinel node (SN) procedure, which is diagnostic in nature, aiming to diagnose if the patient has lymphatic metastasis. Research has shown that every extra lymph node removed during a lymph node dissection, increases the chance on complications [3]. To this end, the procedure differentiates between the first draining lymph nodes (SN) and the following nodes (higher echelons). It is believed that if a patient has metastases, these first draining SNs are the first LNs containing tumour. Therefore in the SN procedure, only the SNs are removed and checked for tumour, opposed to the standard approach of clearing fixed template regions (extended Pelvic Lymph Node Dissection [4]. Furthermore, research showed added value when adding the SN procedure to standard extended Pelvic Lymph Node Dissection, the biochemical recurrence-free survival improves [5, 6]. To SNs are identified preoperatively with SPECT/CT scans. The rough anatomical locations are determined and communicated to the surgeon. Before the operation, the patient is injected with tracer fluid which stains the LNs draining from the prostate. The surgeon looks for the SNs in the patient in the specified regions. However, often not only the first draining LNs are stained, but the higher echelons as well. During surgery, the surgeon must make educated guesses which LNs are the preoperative imaged SNs. This results in inconsistent region classification between pre- and intraoperative results. See Table 1 (cf. 3.3) as an example of the inconsistency in SN location reporting when trying to match the pre and intraoperative SN locations. Being able to link the intraoperatively removed SNs in the patient with the SPECT/CT would aid verification and standardisation of the SN procedure. A routine care friendly solution to bridge the gap between preoperative locations and the intraoperative locations is needed.

The concept of navigation is closely related to the problem stated. Navigation aims to guide the surgeon towards the right SNs during surgery. Preoperative scans are used as roadmaps to guide the surgeon towards the target lesion by projecting the target onto the surgical view with augmented reality [7] and thus provide a link between pre- and intraoperative SN locations. Studies investigating the use of preoperative scans to direct the surgeon are performed in for example penile [8], liver [9], urology [10] and lung surgery. However, these systems assume rigidity of the patient between the preoperative scanning and the surgery. Often, the preoperative scan is made ahead of the surgery and when dealing with soft tissue, deformation of the patient occurs as a consequence of e.g. a different patient orientation, and thus the rigidity assumption does not hold [11].

Dealing with patient deformation in soft tissue surgery is a major challenge in image guided surgery [12]. Research into solving deformations during surgery have been performed on organs such as the kidney [13] and liver [14]. But no solution to solve displacements of SN during Lymph node dissections exists. Using the SN locations as a pattern, much like a fingerprint, an algorithm is developed that pairs preoperative to the intraoperative SN locations. This entails the need for locating the SN locations during surgery. The DROP-IN probe that revolutionised the SN procedure in prostate cancer and has been implemented into the clinic [2, 15-18] is the perfect candidate to pinpoint SN locations. The improved manoeuvrability can be exploited to point out the SNs locations during surgery. The idea of using tracked tooltips to point out landmarks was already proposed in 2000 [19]. However, the introduction of the Drop-In probe and more flexible instruments in robotic surgery have made the tracking of the instrument complicated. A translation into the robotic surgery environment is therefore needed. Previous efforts on tracking the DROP-IN probe used the width of the segmented markers to determine the 3D location of the probe [20]. This thesis presents a novel method to use video-based stereo tracking of the drop-in probe to record SN locations during surgery and investigates the use of an IMU sensor to capture endoscope.

1.2 Research questions

This thesis aims to answer the following questions:

1. Does stereoscopic tracking allow us to capture the pattern needed for registering the preoperative volume to the intraoperative volume
2. Is IMU tracking a viable technique that can be used to track the rotations of the Firefly endoscope
3. Can SN location pattern be used to match the preoperative SN locations to the intraoperative SN locations

The proposed method was validated in a phantom setting and by using clinical data consisting of 13 patient scans.

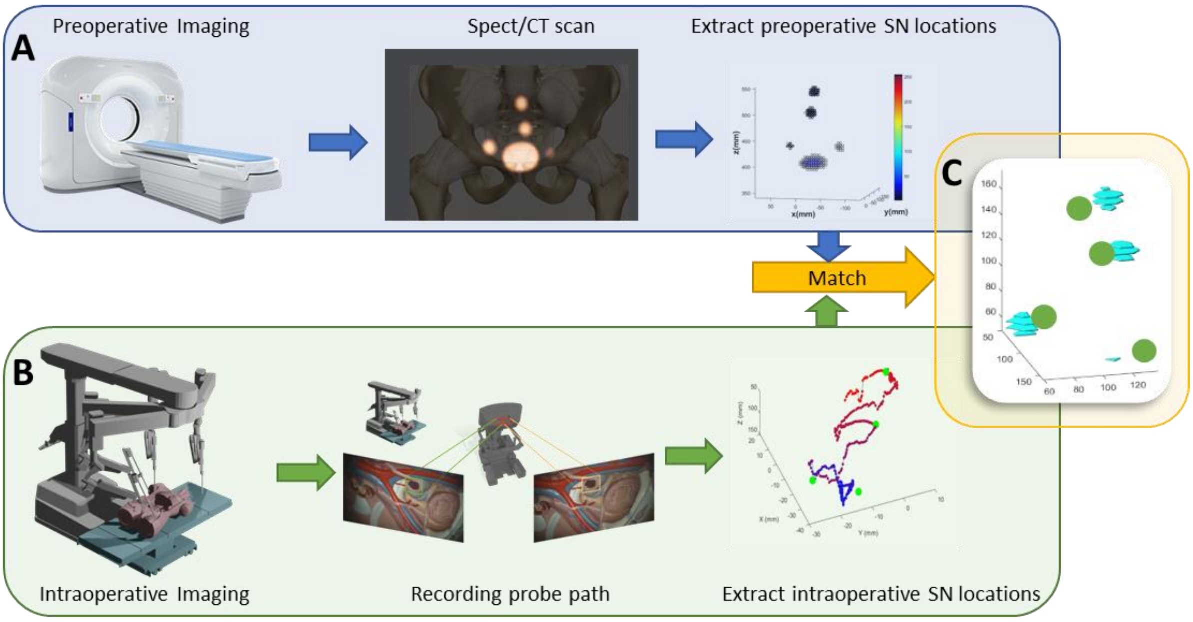

***Figure 1**. Schematic overview of the proposed method. **A)** Building the preoperative SN location volume from the SPECT/CT scans. **B)** Building the intraoperative SN location volume during the surgery. **C)** Register the locations of preoperative SN location volume with intraoperative recorded SN location volume to validate the surgical procedure and link the dissected SN locations to the preoperative SN locations.*

1.3 Thesis structure

The structure of this thesis is structures as follows. Chapter 2 introduces the materials and existing techniques in. Chapter 3 describes the design and implementation of the method required for the method proposed. In chapter 4 the calibration protocol and intermediate results needed for tracking the probe are discussed. In chapter 5 the design and results of experiments that validate the proposed method are presented. Chapter 6 provides a discussion and conclusion.

Chapter 2
Background Methods and Materials

This chapter provides the background of used algorithms and concepts where first the concept of navigation and its application in guided surgery is reviewed, and next methods for volume registration are explained.

2.1 Algebra

To record the location volumes, a single coordinate system is needed, where to locations are placed with the correct distance in between, and the topology is preserved. In computer graphics, an object's location in a coordinate system can be described by a translation and a rotation. The translation is a vector consisting of 3 values: the x-coordinate, y-coordinate and z-coordinate. Every orientation can be described using 3 angles: yaw (ϕ , rotation around z-axis), pitch (θ, rotation around y-axis) and roll (ψ , rotation around x-axis). These 3 angles can be transformed into a rotation matrix with the following formulae:

$$Rx(\psi) = \begin{bmatrix} \cos(\psi) & -\sin(\psi) & 0 \\ \sin(\psi) & \cos(\psi) & 0 \\ 0 & 0 & 1 \end{bmatrix}. \quad (1)$$

$$Ry(\theta) = \begin{bmatrix} \cos(\theta) & 0 & \sin(\theta) \\ 0 & 1 & 0 \\ -\sin(\theta) & 0 & \cos(\theta) \end{bmatrix}. \quad (2)$$

$$Rz(\phi) = \begin{bmatrix} 1 & 0 & 0 \\ 0 & \cos(\phi) & -\sin(\phi) \\ 0 & \sin(\phi) & \cos(\phi) \end{bmatrix}. \quad (3)$$

To create one rotation matrix, the three separate rotation matrices are multiplied together. Different standards for the sequence of the multiplication exist, but the Z*X*Y sequence is most used.

$$R = Rz * Ry * Rx. \quad (4)$$

Given two rotation matrices P and Q, the angle between the two vectors that would be the result from multiplying $P \cdot \vec{v}$ and $Q \cdot \vec{v}$ can be calculated with the following formula:

$$T = \cos^{-1}\left(\frac{trace(P * Q^{-1}) - 1}{2}\right), \quad (5)$$

with Q^{-1} is the inverse of rotation matrix Q.

The translation vector T and rotation matrix R can be combined to form the 4x4 transformation matrix (formula 6) that describes the position and orientation of an object in a coordinate system.

$$\begin{bmatrix} R_{00} & R_{01} & R_{02} & T_x \\ R_{10} & R_{11} & R_{12} & T_y \\ R_{20} & R_{21} & R_{22} & T_z \\ 0 & 0 & 0 & 1 \end{bmatrix} \quad (6)$$

When an object's position A is known relative to an object B that is described in a coordinate system C, then the position of A relative to C can be found by multiplying B by the inverse of the 4x4 transformation matrix of A.

2.2 Tracking modalities

Building the intraoperative volume containing the SN locations entailed tracking the probe to identify SN locations. Two of the conventionally used tracking modalities are optical tracking (OTS) and electro-magnetic tracking (EMT). These two methods will be described below. Different techniques to track instruments during surgery exist, such as optical or electromagnetic tracking systems.

2.2.1 Electromagnetic tracking

EMT generates an electro-magnetic field with a volume of about 1 m^3 in which a target (coil) can be located by induced voltage. The coil can be placed on the surgical tool tip, which makes it a good option for tracking flexible tools. Downsides of EMT are that the tracking field is relatively small compared to OTS, the coils need to be built into the surgical tools, and ferromagnetic objects introduce field distortions [21] which leads to errors in tracking. Ongoing research involves the application of EMT in the OR [22, 23].

2.2.2 Optical tracking

Near-infra red tracking

OTS uses the optical spectrum to track objects. A recognisable marker is placed on the instrument to track with a camera. A widely used form of OTS is near-infra red tracking, which uses reflective spheres as a marker to recognise in 3D space. Near infra-red tracking is highly accurate tracking with a large tracking field; a downside is that it requires a direct line of sight to the markers, which is not feasible when dealing with flexible tools, or the DROP-IN probe.

Visual light tracking

Using visible light to track instruments is another option. Extensive research to recognise and track surgical tools using visible tracking solutions have been proposed. Example solutions for tracking surgical tools are based on: tool feature recognition [24], marker geometry [20, 25], tool models [26], machine learning solutions [27] or stereoscopic solutions [28, 29]. An advantage of using visible light to track the instruments is that it does not require an additional sensor (field generator, or near-infra red camera's) to track the instruments. A downside is that these techniques generally obtain lower accuracy and are prone to error due to lighting conditions.

Regarding tool tracking in robot surgery, adding anything extra that needs a direct line of sight, or be placed stationary at a certain distance is complicated to achieve in the operating room. Being able to track surgical tools by extending already present equipment is desired above introducing new equipment on an already complicated robotic OR. Therefore, this thesis researched visual tracking of the DROP-IN probe, and using IMU sensor to track the movement of the endoscope to solve the impracticality of the direct line of sight issue.

2.3 Stereoscopic principle

Until now, the DROP-IN probe has been successfully tracked using marker-based tracking [20]. However, this method can be improved by taking advantage of the two endoscope cameras available when using the Firefly endoscope. Using two cameras enables the ability to measure depth, just like two eyes are needed to see depth. Research in retinal tool tracking has shown that the stereoscopic principle has potential to aid in tracking surgical tools [28, 29]. Stereoscopic tracking uses the difference in pixel location between the left and right image to calculate the depth with respect to the camera. Figure 2 depicts the principle of stereo vision, where the relation described in formula 7 can be used to measure the depth of an object using a left and right image.

$$depth = f\frac{b}{(X_R) - (X_L)}, \qquad (7)$$

where depth is the distance from the camera to the Real-World point in mm, f is the focal length in mm, b is the distance between the left and right camera origin in mm and (X_R, Y_R) and (X_L, Y_L) are the pixel locations of the Real-World Point in the image of the right and left image respectively.

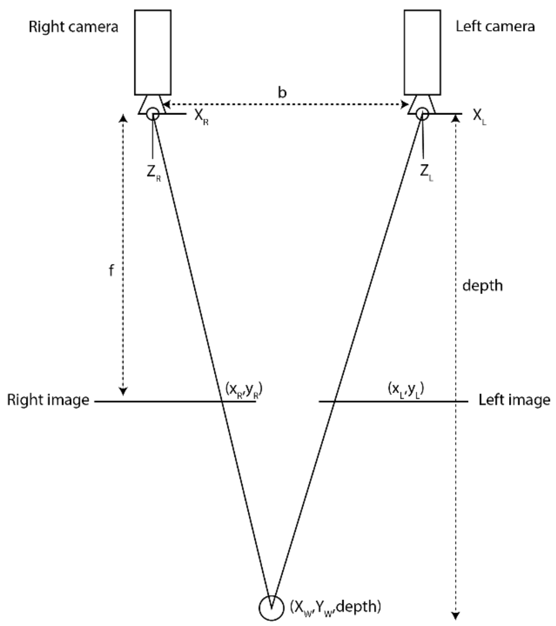

Figure 2. *Stereoscopic depth estimation using the baseline distance between the camera's (b), the focal distance (f) and the difference in pixel locations ((X_R, Y_R) and (X_L, Y_L)) of Real-World point (X_w, Y_W, depth) in the right and left image, to estimate the depth. The ratio of the baseline over pixel location difference is equal to the depth over the focal length of the camera.*

To approximate the focal-length (f) and baseline distance (b), calibration of the camera's is needed. Formula 1 assumes that the left and right image are parallel to each other and that both camera eyes are horizontally aligned such that the difference in pixel locations of the Real Points are only in the x coordinate of between the images. To adjust for imperfect alignment in the y coordinate (one camera is placed a little higher than the other one), a translation can be applied. To adjust for not parallel placement of the cameras in the z direction (one is slightly rotated), rotation and shear transformations are needed to adjust the images.

Next, finding the distance between pixel locations of X_R and X_L (disparity) is an image registration problem between the left and right image. Research is done on the topic of how to create accurate and fast disparity maps. Medical images are notorious for getting inaccurate disparity maps due to low textures and uneven lighting conditions. Machine learning is being tested to research if it can improve disparity map creation in surgical images [30].

The Semi-Global Block Matching (SGBM) algorithm provides a solution to the registration problem [31]. This algorithm aims to match blocks of pixels from the left and right image, minimising the dissimilarity of sub-pixel intensities [32]. The dissimilarity between two pixels x_r and x_l , with intensities I_r and I_l, is specified as:

$$d(x_r, x_l, I_r, I_l) = \max(0, I_l - I_{rmax}, I_{rmin} - I_l), \qquad (8)\ [32]$$

with I_{rmax} and I_{rmin} is the maximal and minimal intensity in the range $x_r - \frac{1}{2} < x_r < x_r + \frac{1}{2}$, where $x_r \pm \frac{1}{2}$ is a linear interpolation between the intensity of x_r and its direct neighbouring pixels (figure 3A).

When all pixels are matched, a disparity map is made, where each pixel $x_{r,}$ is assigned the distance between pixel x_r and x_l, which results in an image of the distance between paired pixels.

Two penalties are introduced to penalise discrepancies in disparity values between two neighbouring pixels. P1 is introduced as penalty for a difference of 1 pixel distance, and P2 for a difference of more than 1 pixel difference in the disparity values. To find the minimal cost disparity values in direction r, the optimisation function consists of 2 terms. Term $C(p, d)$, which is the cost of disparity d in pixel p (dissimilarity formula 8).

$$L_r(p, d) = C(p, d). \quad (9)$$

The second term is a minimisation of the cost of a disparity value of the neighbour of pixel p in direction r (p – r). There are three options for the disparity value of p-r, either it has the same disparity value as in pixel p which introduces no extra penalty,

$$L_r(p - r, d). \quad (10)$$

Or p-r has a 1 distance discrepancy which introduces penalty P1,

$$L_r(p - r, d \pm 1) + P1. \quad (11)$$

Or the discrepancy is bigger than 1 which introduces penalty P2 where disparity i minimises the cost path further in direction r.

$$min_i\big(L_r(p - r, i)\big) + P2. \quad (12)$$

Recursive formula 13 shows the formula that can find the cost of a minimal cost path in direction r.

$$L_r(p, d) = C(p, d) + \min\big(\ L_r(p - r,\ d),\ L_r(p - r, d \pm 1) + P1,\ min_i\big(L_r(p - r, i)\big) + P2\ \big). \quad (13)$$ [31]

To find the final cost of a disparity map, function L_r is summed over multiple directions.

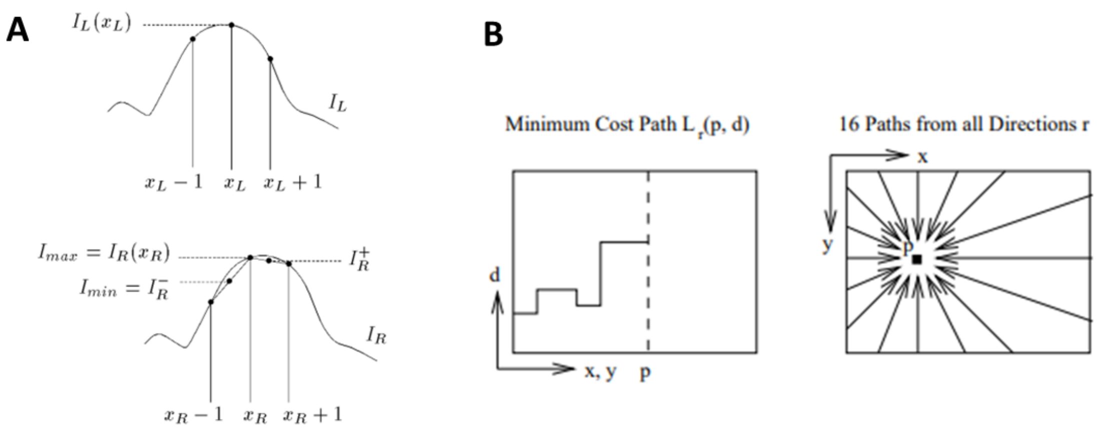

Figure 3**. SGBM disparity map calculation.* ***A) *The intensity function in and around pixel IL and IR. This function is used to describe the dissimilarity between pixel I_L and I_R , where the pixel intensity in I_L is compared to the highest and lowest intensity in the function of I_R and the subpixel intensity between I_R -1 and I_R +1 [32].* ***B)*** *The path that minimises the dissimilarity function and discrepancies in disparity [31].*

2.4 IMU sensor

This thesis investigated the possibility of using a 6 axis IMU sensor to track the camera movement during surgery. Therefore, a background of the workings of an IMU sensor is provided. When the probe is tracked with the Firefly endoscope, the 3D locations of the SNs are with respect the virtual camera point of the endoscope. However, during surgery, the endoscope will change angels and depth such that the surgeon has a good view of the dissection site. A fixed point is 3D is needed to maintain the spatial information between the SNs recorded under different Firefly positions and orientations. To accomplish this, the Firefly itself must be tracked with respect to a fixed point.

A IMU sensor could be used to track the Firefly camera. The 6 axis IMU sensor consists of an accelerometer and gyroscope. The accelerometer is a sensor that can capture its acceleration in x, y, and z direction (m/s^2) and the gyroscope can measure the speed of rotation in radial velocity (degrees/s) around its x-, y- and z-axis. When stationary, the accelerometer measures the gravitational pull of earth. Using this, the relative orientation of the sensor can be calculated with respect to earths centre. The rotation in the XY-plane (the plane perpendicular to gravity) cannot be determined. This rotation can be measured with the gyroscope. By assuming constant velocity between the measurement intervals, this rotation can be found by integrating over the rotation speed.

Displacement can be obtained by assuming constant acceleration between measurements of the accelerometer. However, because of the nature of the sensors, measurements of the sensor fluctuate slightly over time. The displacement is then calculated by double integrating over the acceleration measurements. However, due to the double integration, the earlier mentioned small fluctuations will contribute to significant errors in the displacement calculation when integrated over a long period of time. Getting an accurate displacement using only IMU sensor data is difficult to accomplish. Therefore, often IMU sensors are combined with other modalities that recalibrate the position after a period (think of GPS).

2.5 Volume registration algorithms

After the intraoperative and preoperative volume were recorded, the matching of the SN locations was done using a registration algorithm that intends to find a transformation matrix that registers a template volume to the reference volume. The most basic registration algorithm is Iterative Closest Point (ICP) [33], which minimises least squares by iteratively computing the closest points between the reference and template volume. Using the closest pointset and reference pointset, the optimal rotation under least squared is found using Singular Value Decomposition [34]. The translation is found aligning the centre of mass of the two pointsets. The template points are updated using the found rotation and translation and a new closest correspondence between the template and reference pointset is calculated. This is repeated until the change in mean square error falls below a chosen threshold. ICP algorithm is a basic registration algorithm. However, because ICP uses the least squares method to find the translation and rotation to minimise the distance, outliers affect the mean used in the minimisation, thus the algorithm is prone to outliers in the point set.

Two other widely used registration algorithms are Chamfer matching [35] and Coherent Point Drift (CPD) [36]. Chamfer matching is a robust [37] and widely used image registration algorithm in medical applications [38-41]. To accomplish this, the algorithm transforms the template image to a landscape of distances, where each voxel value is the Euclidean distance from this voxel to the nearest voxel that is part of an edge. To identify the transformation matrix that matches the two volumes, the sum of the distances hit by the template volume in the reference volume needs to be minimised (figure 4). The algorithm iteratively applies transformations and rotations with a specified step size to find the transformation that results in a minimum distance score.

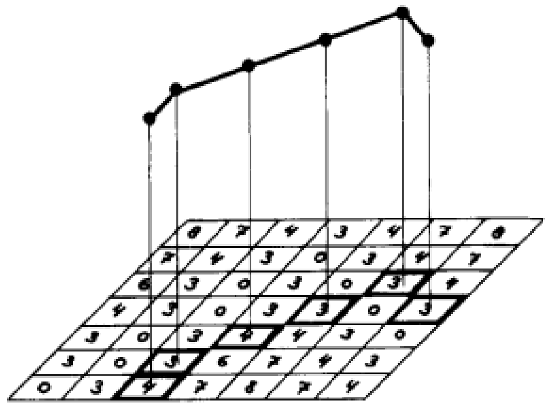

Figure 4*. Template volume pixels hit the distance transform pixels from the reference volume. [35]*

To reduce computational load, a resolution pyramid is used. Chamfer matching is first applied to the lowest resolution reference image. When the optimal position of the template volume registered to the reference volume is found, the algorithm repeats with a higher resolution reference volume. The local minima found is used as a start position of the algorithm in the higher resolution reference image.

Coherent Point drift makes uses of gaussians mixed models to register a template volume to a reference volume. This algorithm models the data in the template volume as gaussian distributions. Next, it uses expectation maximisation to find the translation and rotations, such that the likelihood the assigned gaussian distributions are moved with respect to the datapoints such that the likelihood of the data is generated from the gaussian distributions is maximized.

Chapter 3

New method and implementation

The proposed method consists of three key steps. The first step is to isolate the preoperative SN locations from the scans. The second step is to use the tracking of probe to record the locations of dissected SNs, while preserving the topology and distance between the SNs. The third step is to match the two created volumes and link the preoperative to the intraoperative locations.

3.1 Programming environment

The programming languages used to prototype the proposed method are C++, MATLAB and python. C++ was used for tracking the probe in surgical images. MATLAB was used for programming the registration algorithms. Python was used to read out the IMU sensor data. For the tracking software, the OpenCV library [42], and imufusion [43] library was used. For the ICP and CPD registration algorithms the MATLAB Computer Vision Toolbox™ implementations were used. Most of the analysis and all the tracking was done on the CPU of a laptop with an AMD Ryzen™ 7 4800H CPU @2.90 GHz. A part of the registration algorithm analysis was performed on the CPU of a desktop computer with an Intel® Core™ i9-10900X @3.70 GHz.

3.2 Phantom creation

Surgery on a phantom model was conducted with the Da Vinci robot (Intuitive Inc. Sunnyvale, US), with the stereoscopic Firefly endoscope (Intuitive Inc.). The phantom model is an educational anatomical model. The intestines were removed to create an abdominopelvic cavity in which four ^{99m}Tc sources (300 KBq) were placed. Using the SIEMENS NG4-SymbiaT6, a SPECT scan (128x128x76) was made to image the ^{99m}Tc sources, with slice thickness of 4.795mm. Alongside the SPECT, a CT scan (512x512x182) was made with slice thickness of 3mm.

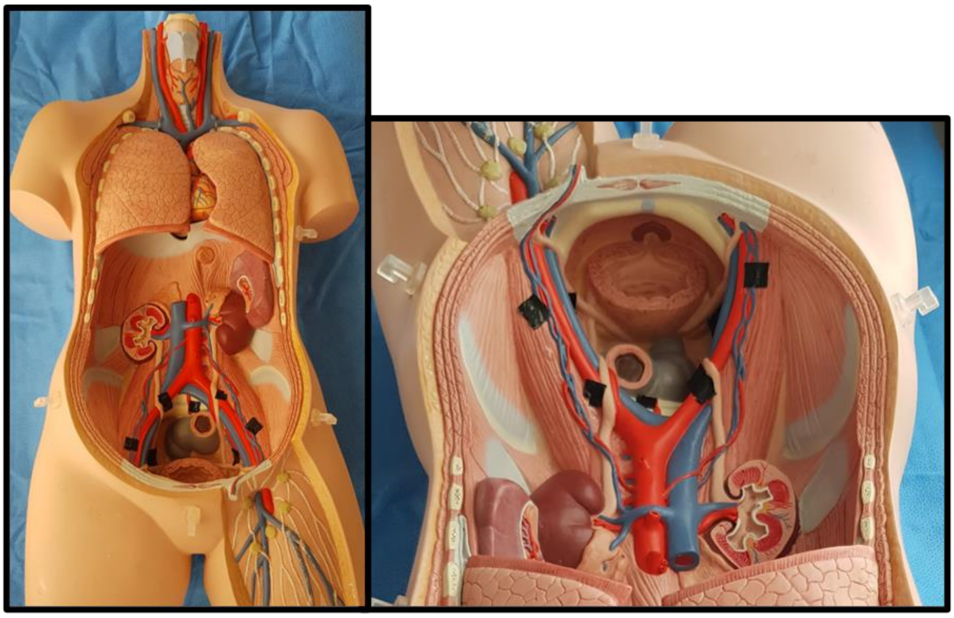

Figure 5. *The educational anatomical doll used in the phantom experiment. The black dots are the regions where commonly SNs are located that drain from the prostate.*

3.3 Clinical data

The data of the 13 patient scans was anonymised and only patients that gave permission for research participation were included in the study. All patients underwent SN accompanied with an extended Pelvic Lymph Node Dissection. The median number of nodes identified on the preoperative SPECT scan was 5, the median number of removed SNs in the SN procedure was 4.

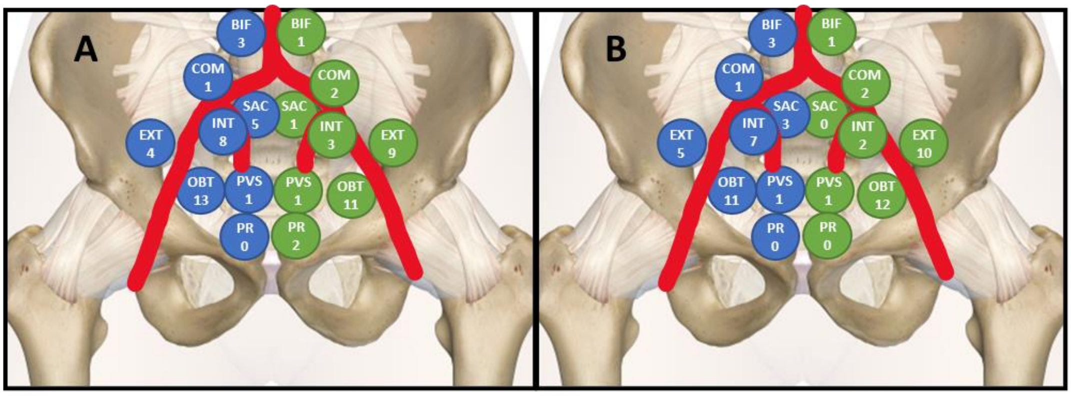

Figure 6. *SN locations in scan, classified in the following left (green) and right (blue) anatomical regions: Common bifurcation (BIF), presacral (SAC), common Iliac (COM), external Iliac (EXT), internal Iliac (INT), pararectal (PR), paravesical (PVS) and obturator (OBT).* ***A)*** *The preoperative SN locations.* ***B)*** *The reported intraoperative SN locations.*

Patient number	SN imaged	SN removed	Manual applied changes of postop locations based on preop locations (from -> to)		Pre and postoperative locations match (+ extra, - missing)	
Patient 1	3	3	n	-	y	-
Patient 2	5	4	n	-	n	+ OBT R - SAC&PR
Patient 3	4	4	y	Cloquet R -> OBT R	n	+ OBT R - PR
Patient 4	3	3	y	Marcille R -> OBT R SAC R -> INT R	y	-
Patient 5	6	6	y	EXT L -> COM L Marcille R -> INT R PVS R -> OBT R	n	+ OBT R - INT L
Patient 6	5	5	y	PR R -> OBT R PAR L -> OBT L	y	-
Patient 7	7	9	y	OBT R -> INT R EXT R -> BIF R	n	+ EXT L&OBT L
Patient 8	6	6	y	OBT R -> PVS R OBT R -> INT R EXT R -> BIFR R PR L -> INT L	y	-
Patient 9	5	4	y	EXT L -> INT L	n	- OBT L
Patient 10	4	4	y	EXT L -> OBT L Marcille R-> INT R OBT R -> EXT R	y	-
Patient 11	5	5	y	PR R -> INT R Marcille R -> BIFR R EXT L -> BIFR L	n	+ EXT R - SAC L
Patient 12	7	7	y	PR -> OBT L Ureter L -> OBT L Prostate L -> OBT L	n	+ OBT L - INT R
Patient 13	5	4	y	EXT R -> INT R INT R -> SAC R	n	- SAC L

Table 1. *Patient SPECT scan data. Reported is the number of imaged SNs preoperatively, the number of SNs removed during the SN procedure. Also, if a manual interpretation that was done to try to match the pre- and intraoperative locations are reported. Lastly, if after the manual changes the postoperative locations match the preoperative locations is reported (extra SN removed and SN missed or skipped in the surgery).*

To obtain the lymph node locations from preoperative scans, the scans were loaded into RadiAnt™. The SNs were identified by using the annotations from the radiologist report. The activity was manually scaled until a good separation between higher echelons and SNs was visible, and the activity was segmented out. K-means clustering was applied to get the centres of the activity regions. The classification was manually checked and adjusted if the clusters did not comply with the radiologist reports.

3.4 Probe tracking

The gamma probe is used to scan tissue for activity readings that indicate SNs in the patient. Therefore, the probe can be used to point out the LN locations. By tracking the probe, the intraoperative SN locations can be recorded. A new generation of DROP-IN probe (CLICK-ON probe [44]) was used to measure the activity and point to the SN locations. To track the probe in the camera view, a stereoscopic tracking algorithm was introduced. This algorithm extended on a previous solution which used three rectangular markers to locate and triangulate the position of the drop-in gamma probe in 3D [20]. Our stereoscopic tracking algorithm used these markers to recognise the drop-in probe in the surgical video, and used functionality provided by the stereovision functions from OpenCV library to extract 3D coordinates from the images.

3.4.1 Video-based marker tracking

Current tracking software for the DROP-IN probe makes use of markers [20]. Three stripes are placed on the probe. A rectangle is fitted around these markers. The long side of the rectangle is used as an approximation of the line through the middle of the probe. Because the width of the probe is known, the pinhole model is used to transform the pixel locations to 3d coordinates. A flow of this approach is that during the tracking of the probe a perfect segmentation of the probe markers is assumed, and that half of the marker is always completely in view. This method fails with imperfect segmentation due to obstruction of the markers or with different lighting conditions.

3.4.2 Video-based stereo tracking

The tracking of the probe was done preoperatively. The video output of the Davinci robot was recorded using a recording program that used multithreading to capture frames. Together with each frame, a timecode was stored such that the individual frames of the left and right eye could be matched postoperatively. To match the frames, a sub-optimal algorithm was implemented that kept the difference in time between left and right frames below 15 milliseconds (ms). If the difference became larger than 15ms, frames were skipped until the difference was again smaller than 10ms, or the difference started increasing again. In general, this resulted an average of -1±4ms time difference between the two left and right eye frames. This difference in time is acceptable in this application, as the probe was kept stationary when the surgeon pointed at a lymph node. Consequently, a few milliseconds difference between left and right frame does not result in a different position of the probe between the two frames.

The 3 stripes marker tacking was extended to improve tracking results using the stereoscopic principle. The stereoscopic tracking uses three coloured rectangular markers to recognise the probe in the video frames. Instead of using the markers width to determine depth, the stereoscopic principle was used to determine the depth of the marker. The find the disparity map needed for measuring depth, the SGMB algorithm was used. To lower the time needed to find the disparity map, the probe was cropped out of the image. The disparity map was calculated from the cropped frames. Next, the pixels within the marker area of the probe, the disparity values were set to the median of the disparity values within the marker area. The cropped disparity map was placed back into the full image. OpenCV reprojectImageTo3D was used to find the 3D coordinates in mm.

3.5 Firefly tracking

To track the Firefly camera, a LSM6DSOX IMU sensor consisting of an accelerometer (sensitivity of $0.122*10^{-3}$ m/s^2), a gyroscope (sensitivity of $4.375*10^{-3}$ degrees/s) and an Arduino Nano Every (Arduino Inc.) were placed in a custom 3D printed mount. The Arduino was connected to a laptop which used software [43] that can read the data from the IMU sensor and returns its rotation angles. During surgery, the camera rotates and moves to keep surgical tools in view. The stereoscopic tracking algorithm could record the SN locations with respect to the **Firefly** origin (Figure 7, ${}^{Firefly}T_{SN}$). However, the **Firefly** origin moves during surgery. To register the SNs to the intraoperative volume, the location of the SN with respect to the patient needed to be calculated. As the camera is inserted through a trocar in the patient’s belly and rotates around this fixed insertion point, the **Trocar** was used as a reference point. To relate the recorded SN locations to the **Trocar**, two transformation matrices needed to be calculated.

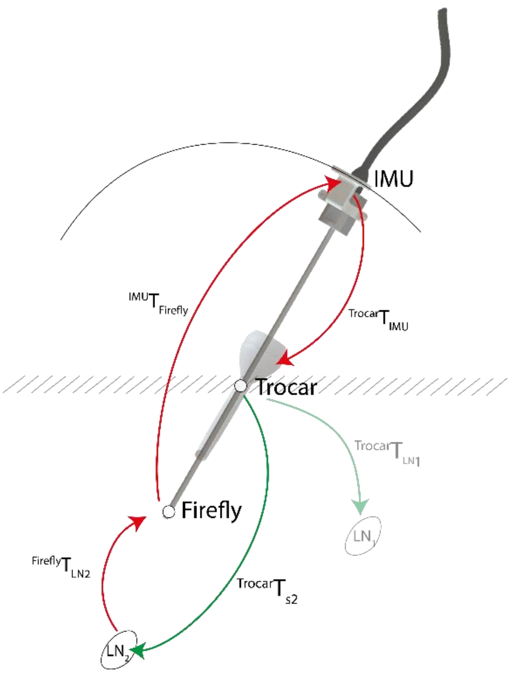

Figure 7. *Transformations needed to relate SN locations to the fixed rotation point. Using transformation matrices* $^{Firefly}T_{SN2}$, $^{IMU}T_{Firefly}$ *and* $^{Trocar}T_{IMU}$, *the position of the SN with respect to the Trocar were calculated.*

3.5.1 $^{IMU}T_{firefly}$ Transformation matrix Firefly origin to IMU sensor

Using the IMU sensor, the IMU sensor was used to track the orientation and movement of the camera. Figure 8A shows a schematic of the calibration of the transformation matrix $^{IMU}T_{Firefly}$. Assuming that the sensor is placed back in the exact same place, this calibration calculates a fixed distance from the IMU sensor to the Firefly origin.

To relate the IMU sensor to the Firefly origin, the distance of edge (**IMU, Firefly**) needed to be calibrated. Software was used to track the IMU sensor, which calculates the angles ψ, θ and φ (yaw, pitch and roll) with respect to gravity and initial orientation of the IMU sensor. To find angle **T** (the angle between the two recorded IMU orientations), the three angles of the IMU sensor at time t and t+1, were transformed to a 3x3 rotation matrix using formula 1, 2, 3 and 4 (chapter 2).

Using the rotation matrix R_t, and R_{t+1} in sensor position IMU_t and IMU_{t+1}, the angle **T** between these two orientations was calculated using the formula for distance between rotation matrices (formula 5). The distance from the **IMU** sensor to the **Trocar** $(IMU, Trocar)$ was calculated using formula 9 (chapter 2).

$$(IMU, Trocar) = \frac{0.5 * l}{\sin(0.5 * T)}. \quad (14)$$

Next, a setup was used where the distance between the **Trocar** and spot **S** was known. The distance of ($Trocar$,Firefly) was calculated, using this known distance, and the coordinates of **S** with respect to the Firefly origin.

$$(Trocar, Firefly) = \sqrt{(Trocar, LN)^2 + {S_{XY}}^2} - S_Z. \quad (15)$$

The translation distance between $(IMU, Firefly)$ was found by adding the results from formula 14 and 15.

The rotation was approximated by visually aligning the axis on the IMU chip with the x and y axis in the Firefly endoscope view, such that the rotation part of the calibration matrix was equal to the identity matrix. This is a rough approximation of the rotations needed to relate the IMU rotations to the Firefly origin orientation.

3.5.2 ${}^{Trocar}T_{IMU}$: Transformation matrix IMU to trocar

The transformation matrix from the IMU sensor to the Trocar changes when the surgeon moves the Firefly. The transformation matrix from the IMU to the Trocar (${}^{Trocar}T_{IMU}$) was calculated by manually measuring the distance between IMU sensor and the Trocar. The transformation matrix is the result of multiplying this distance with the angels measured by the IMU sensor (see figure 8B).

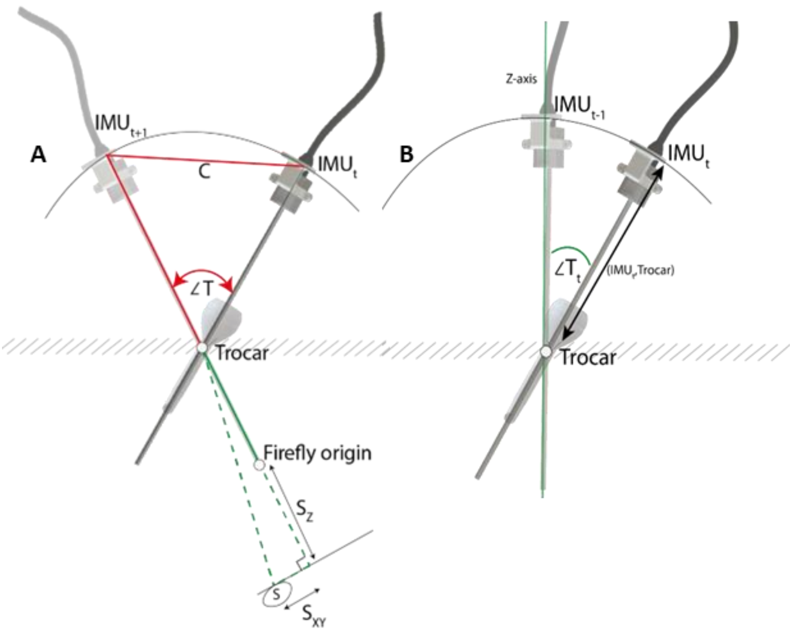

Figure 8**. Calibration of IMU sensor to Virtual Camera Point and tracking the firefly with respect to the trocar.* ***A) *Calibration of the camera to the IMU sensor. R is rotating point,* $\boldsymbol{IMU_t}$ *is the sensor at time t and* $\boldsymbol{IMU_{t+1}}$ *is the sensor at time t+1,* ***C*** *is distance travelled by the IMU,* ***T*** *is angle travelled by the IMU,* ***Firefly*** *is the origin of the endoscope coordinate system,* $\boldsymbol{S_z}$ *is Z coordinate of spot* ***S*** *with respect to the Firefly origin,* $\boldsymbol{S_{xy}}$ *is the distance from the Firefly origin to spot* ***S*** *in the XY plane.* ***B)*** *The IMU sensor records angles* $\boldsymbol{\angle T_t}$ *with respect to the* ***Z-axis****. Given the IMU sensor position at location* $\boldsymbol{IMU_t}$ *at time t, we can model the IMU sensor positioned along the* ***Z-axis*** *of the trocar at* $\boldsymbol{IMU_{t-1}}$*. At this point the IMU coordinates are (0, 0, d) where d is the distance of the sensor to the Trocar (*$\boldsymbol{IMU_t}$*,* ***Trocar****). To get the position of* $\boldsymbol{IMU_t}$ *with respect to the* ***Trocar****, the location of* $\boldsymbol{IMU_{t-1}}$ *was multiplied by the rotation matrix derived of the angles of* $\boldsymbol{IMU_t}$ *(*$\boldsymbol{\angle T_t}$*).*

3.6 Registration algorithm implementation

3.6.1 Location volumes

From the location coordinates returned by the probe tracking software and the centres of k-means clustering, the two volumes are created by generating a filled sphere with diameter of 10mm around coordinates in the two separate volumes. Research suggest that pelvic SNs are generally smaller than 10mm [45] and the diameter of the gamma probe is 10mm, so this size was chosen to generate the spheres in the location volumes.

3.6.2 Registration algorithm implementation

To register the scan location (template) to the intraoperative locations (reference), for the phantom study, only translations and rotations are considered. To decrease the search space of different possible rotations and translation, a maximal translation and rotation was implemented. Because the SNs are labelled based on the anatomical location, it was assumed that a first manual registration within a margin of 6 cm and 60 degrees from the optimal registration could be. A MATLAB tool was created to rotate and translate the preoperative locations to manually make the first rough registration and use this as the start position for the chamfer matching algorithm. For the ICP and CPD algorithm, the standard MATLAB implementation in the Computer Vision toolbox was used.

After the preoperative and intraoperative volumes were registered, nearest neighbour was used to pair the pre-operative locations with the intraoperative locations.

Chapter 4

Calibration and intermediate calibration results

4.1 IMU sensor – Firefly origin calibration

To calibrate the distance between the IMU sensor and the Firefly origin, two measurements were needed. First the distance of the IMU to the Trocar can be determined, by first fixing the robot arm with the Firefly endoscope, such that the distances between the IMU and Trocar, and Trocar and Firefly origin do not change.

The first measurement entailed recording the displacement and orientation angles of the IMU sensor, while the robot arm was moved in a spherical motion around the trocar. Using the geometry, the displacement between separate measurements and the angle of the IMU sensor could be used to continuously estimate the distance. Figure 9 and table 2 shows the results of this measurement. A threshold was applied to the data, such that only the readings where the IMU sensor moved more than 1 mm and with a bigger orientation change than 1 degree. This resulted in 452 mm median ([416,488] mm interquartile). This result showed that using the IMU sensor displacement is not exact enough. The difference between the lower quartile and upper quartile amounts to 7 cm. Manually measuring the distance from the IMU sensor to the trocar, resulted in 46 cm. This manually measured distance was used in the calibration of the experiments.

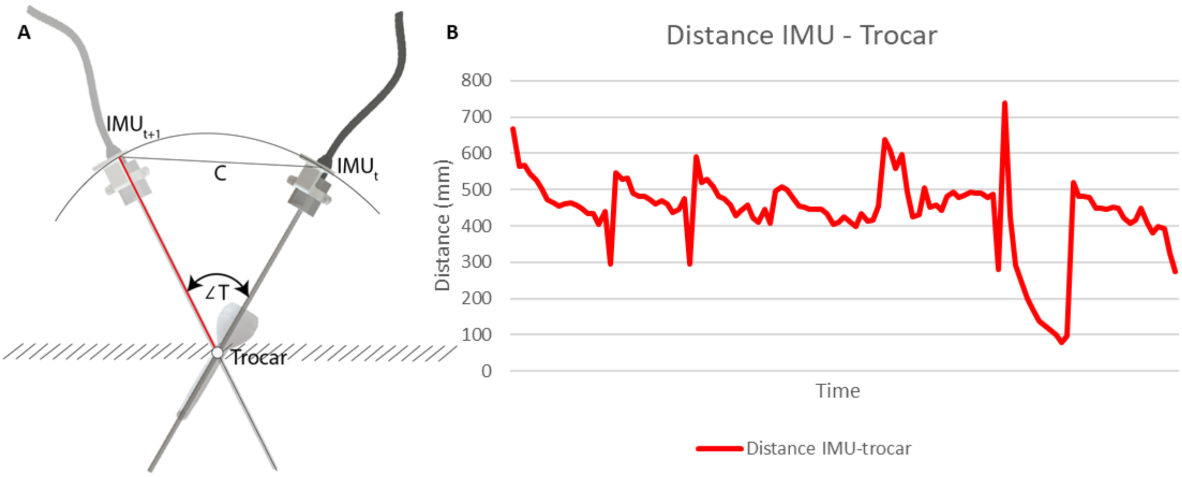

***Figure 9**. Distance between the IMU sensor and the trocar. **A)** Schematic illustration how the distance is calculated as described in chapter 3. **B)** Results of the distance between the IMU sensor and the trocar over time during the calibration experiment.*

	IMU-trocar
Mean (mm)	438
Median (mm)	452
Std (mm)	110
Interquartile [0.25 – 0.75] (mm)	416-488
Manual measurement (mm)	46 * 10^1

***Table 2.** Results of the calibration experiment and a manual calculation of the distance.*

Next, the distance between the Firefly origin and trocar needed to be determined. A setup was created where two markers were placed on a known distance from the trocar. Using the method described in the earlier chapter, geometry was used to find the distance. The distance was measured using different camera orientations, without changing the depth from Firefly origin to Trocar. Figure 10 and table 3 show the results of the calibration. The mean distance was 158 mm ([157-158] mm interquartile).

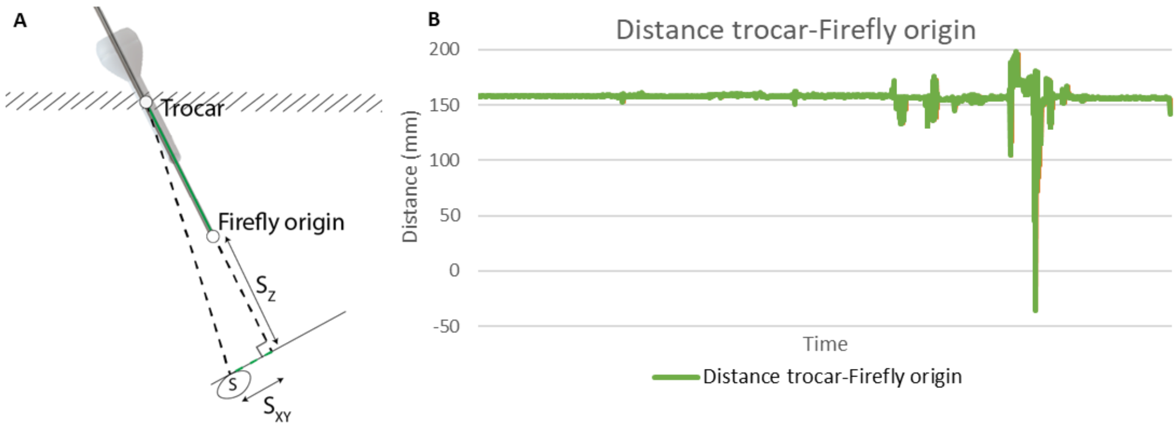

Figure 10. *Distance between the Firefly origin and the trocar.* ***A)*** *Schematic illustration how the distance is calculated as described in chapter 3.* ***B)*** *Results of the distance between the trocar and the Firefly origin over time during the calibration experiment.*

	Firefly-Trocar
Mean (mm)	157
Median (mm)	158
Std (mm)	8
Interquartile [0.25 – 0.75] (mm)	157-158

Table 3. *Results of the calibration experiment to calculate the distance between the Firefly origin and the trocar.*

Adding the manual calibration from Trocar-Firefly origin and IMU-Trocar resulted in a total distance of 62 cm between the Firefly origin and IMU sensor. This distance figures out the translation in the z-coordinate from the IMU sensor to the Firefly origin. By aligning the IMU sensor and the endoscopic view, the rotation matrix needed for the calibration was an identity matrix.

4.2 Firefly internal calibration

4.2.1 Pinhole model

Calibration of the camera is done using the OpenCV calibration example software. This calibration uses a checkerboard pattern to find the intrinsic and extrinsic calibration matrices of the camera. The camera is modelled as a pinhole camera, where each light ray goes through a (pin)hole before it is captured on the image plane. The distance of the pinhole to the image plane is the focal length. The coordinates of the projection of the pinhole onto the image plane is the principal point (cx, cy). The relation between coordinates in an image *m*, and coordinates in the real world *M* is described by the following formula

$$sm = A[R\ t]M, \quad (14)$$

where s is a scaling factor, A is the intrinsic calibration $\begin{bmatrix} fx & 0 & cx \\ 0 & fy & cy \\ 0 & 0 & 1 \end{bmatrix}$, and *[R T]* is a 4 by 4 transformation matrix that relates the world coordinate system and the camera coordinate system (extrinsic calibration) [46].

4.2.2 Calibration

The checkerboard size used was 8 squares high and 11 squares wide, with a size of 10 mm per square. While taking images of the checkerboard pattern, the aim was to try to have the checkerboard pattern span the entire frame. 30 pictures were taken changing position and orientation of the Firefly endoscope. Different sized checkerboards were tested, the board with the lowest reprojection error kept as internal calibration.

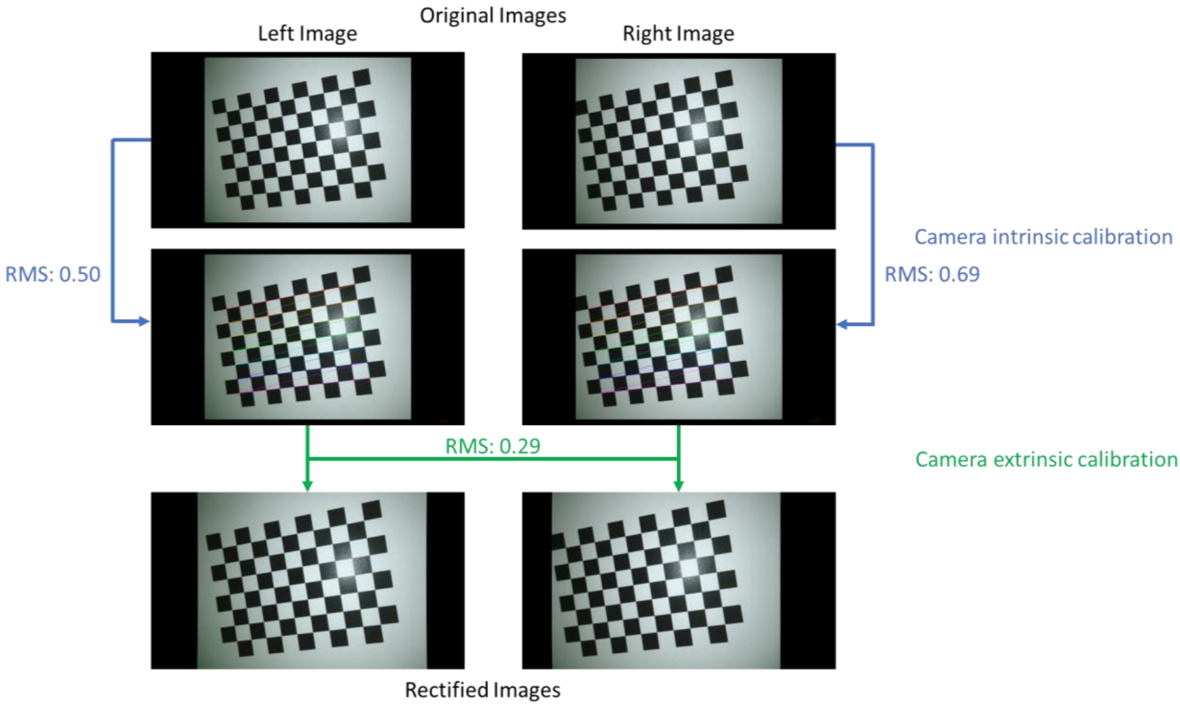

Figure 11. *Firefly calibration results using the OpenCV camera calibration functions.*

The results of the calibration steps and algorithms settings that are not investigated in this thesis can be found in appendix A.

Chapter 5
Experiments and results

5.1 Phantom evaluation

The phantom with the four sources was placed under the Da Vinci robot and subjected to drop-in radioguided target identification. The location where the probe measured the highest activity was stored in a 3D volume as a SN location. After identification of the four sources, the pre-operative volume was registered to the intraoperative volume using an iterative registration algorithm.

The preoperative volume consisted of the scan of the phantom with two sources placed in the right external Iliac and obturator, and two sources in the left external and common Iliac. The probe was tracked whilst the radioactivity counts were measured. When the surgeon was confident the highest activity was being measured, the location of the probe was stored. The Firefly camera was moved between the left and right SN locations. The probe locations were recorded with respect to the trocar using stereoscopic probe tracking, IMU gyroscope data and manually measuring the distance between the IMU sensor and trocar. This procedure was performed twice in total.

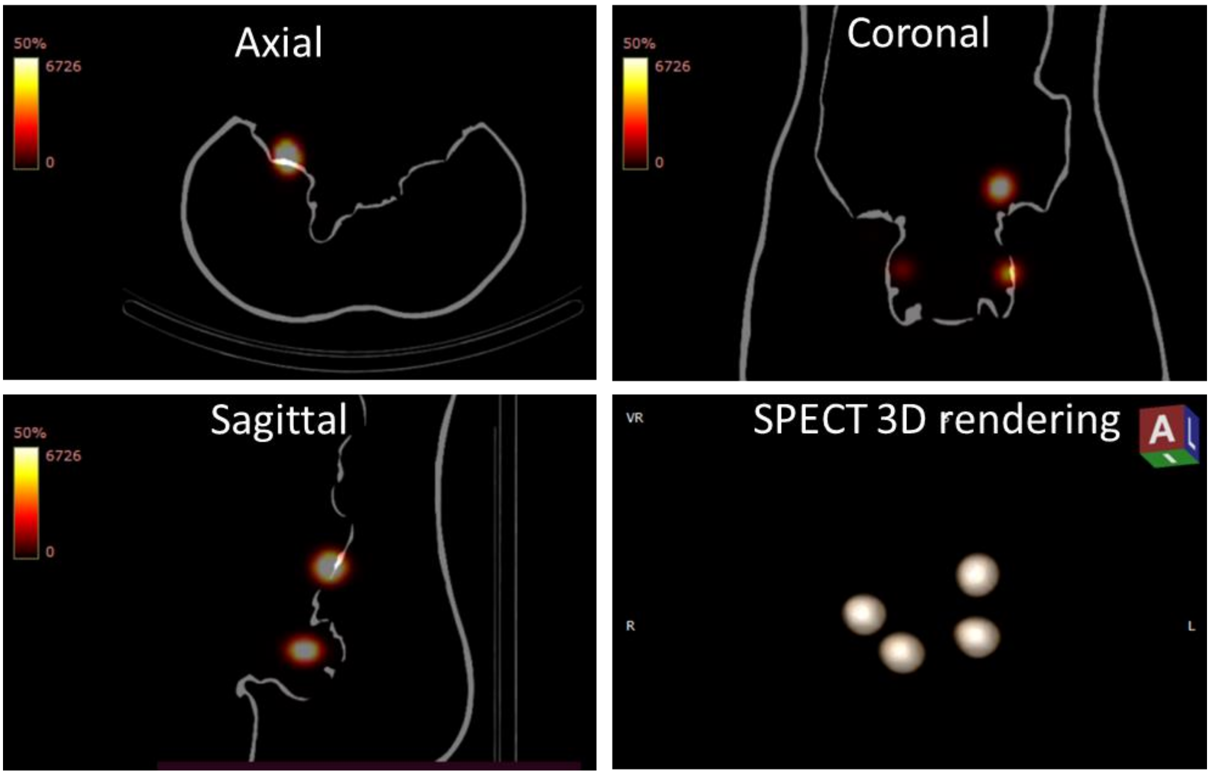

Figure 12. *Visualisation of the SPECT/CT scan of the phantom in Axial (bottom), Coronal (above) and Sagittal (side) view. And a 3D rendering of the SPECT signal in RadiAnt.*

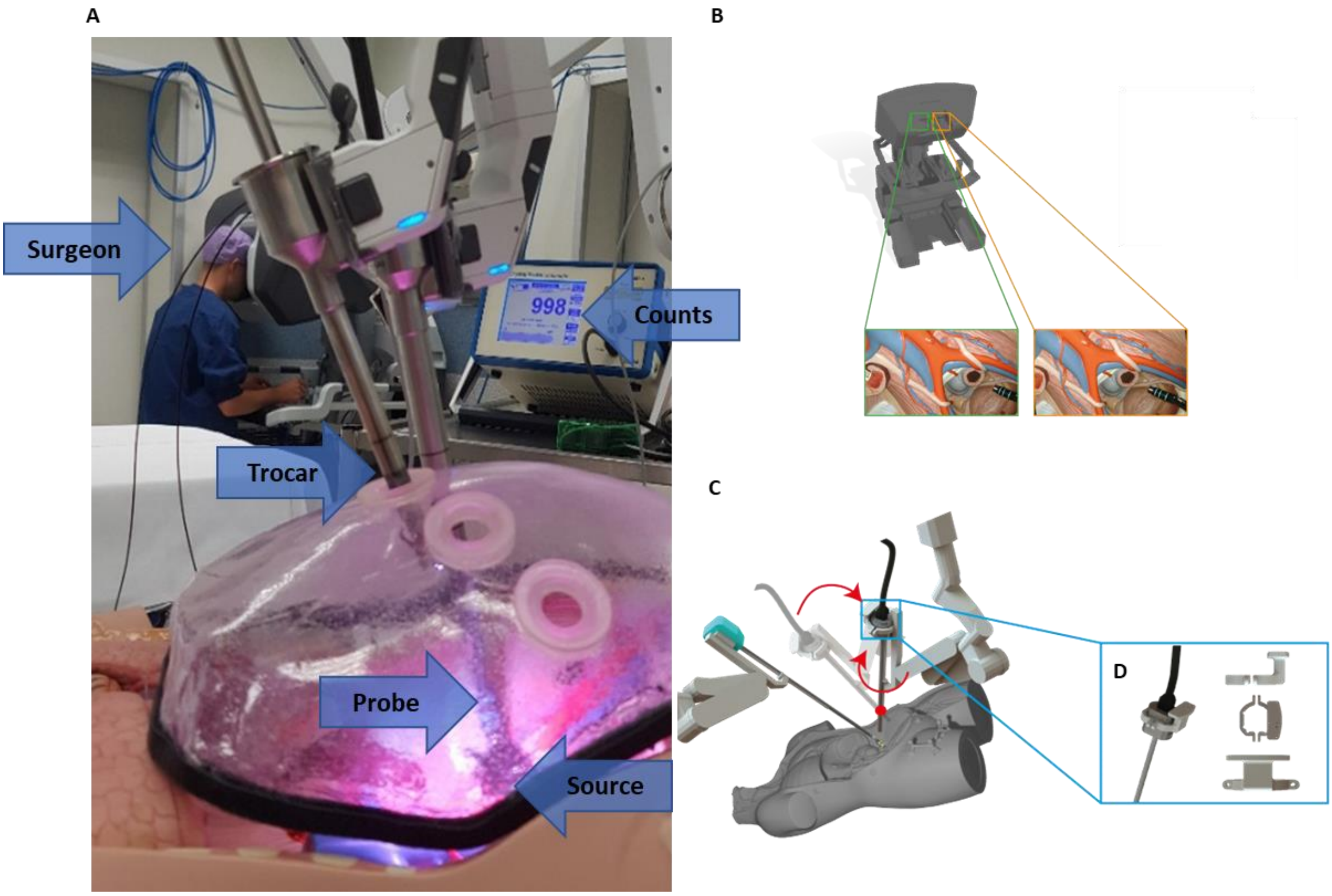

Figure 13. *The tracking experiment setup.* ***A)*** *Overview of the phantom experiment.* ***B)*** *The stereoscopic tracking setup to improve accuracy in and range in tracking the probe. The images are captured from the Da Vinci robot. Ring markers are used to recognise the probe in the images.* ***C)*** *The camera tracking setup showing the movement of the camera around the trocar (red dot).* ***D)*** *A custom 3D printed mount to attach the IMU sensor and Arduino to the Firefly camera. This mount ensures that the IMU sensor is placed in the same location between surgeries.*

5.1.1 Results

This allowed for a chamfer matching registration result obtaining an Root Mean Squared (RMS) distance of 8.9±3.3mm and 11.4±1.6mm between the paired preoperative and intraoperative SN locations.

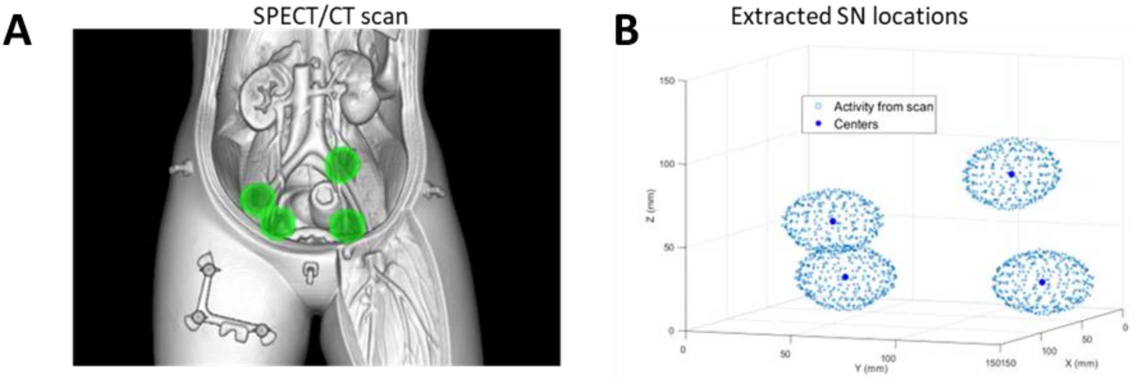

Figure 14*. Results of the preoperative volume from the phantom experiment.* ***A)*** *The SPECT/CT scan of the phantom model with sources placed in the right external and internal Iliac, and in the left external and common Iliac.* ***B)*** *The result of k-means algorithm on the segmented activity of the SPECT scan.*

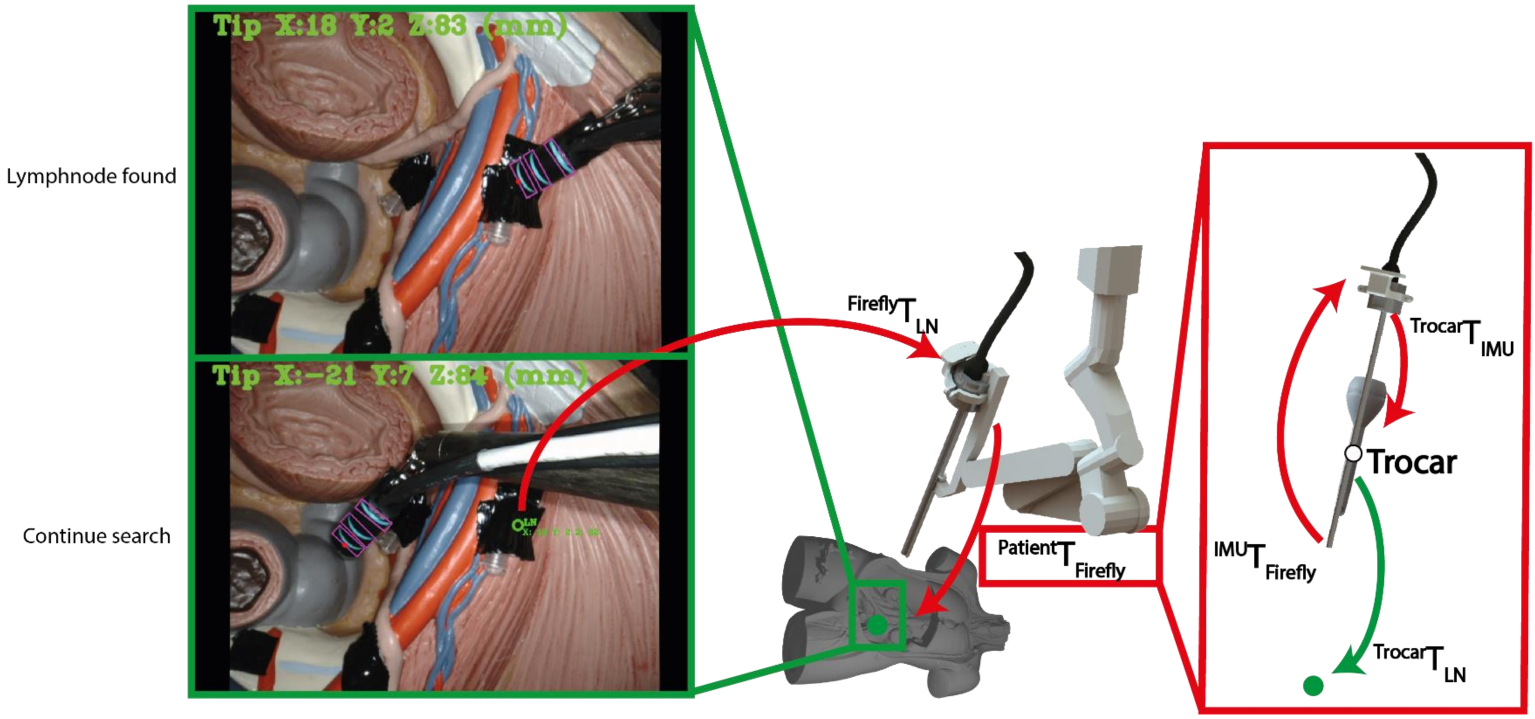

Figure 15*. Results of using stereo tracking to build the intraoperative volume from the phantom experiment.* ***A)*** *The drop in probe is tracked in the surgical video. The recorded location is related to the patient volume via the transformation matrices.* ***B)*** *To register the SN locations to the patient, the SN locations with respect to the Trocar were calculated with the transformation matrices.*

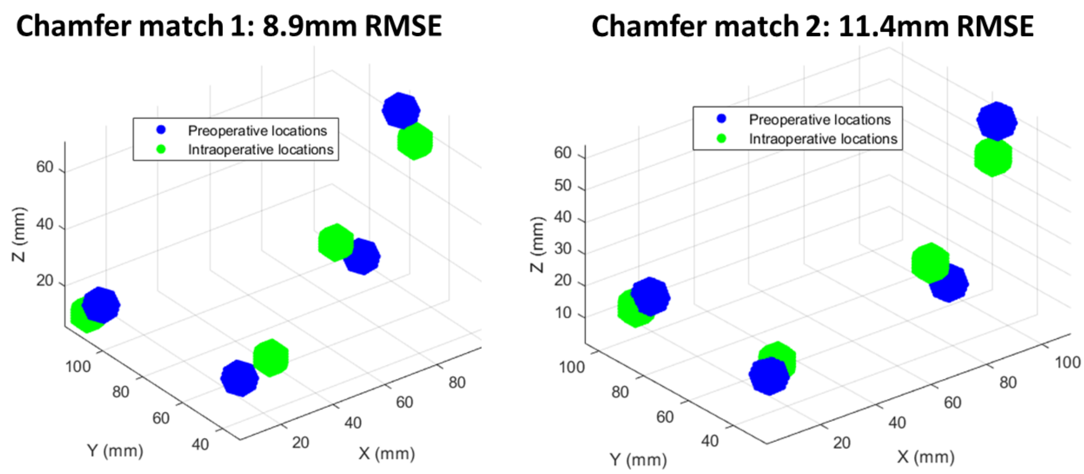

Figure 16. *Chamfer matching volume registration result. The preoperative volume is registered to the intraoperative volume. nearest neighbour paired the preoperative with the intraoperative SN 100% correctly. The RMS distance after volume registration between the linked SNs in the first and second try was 8.9 ±3.3 mm and 11.4 ±1.6 mm respectively.*

5.2 Accuracy marker tracking vs stereo tracking

To validate the accuracy and precision of stereoscopic tracking versus marker tracking, an experiment was performed where the position of the probe was recorded using known intervals of 4 cm. The root mean squared (RMS) and standard deviation (std) of the difference between reported distance travelled of the tracking algorithms and the known travelled distance was reported. Per location of the probe, the median of 60 analysed frames was taken to determine the location of the stationary probe. The precision was determined by reporting the std among these 60 frames.

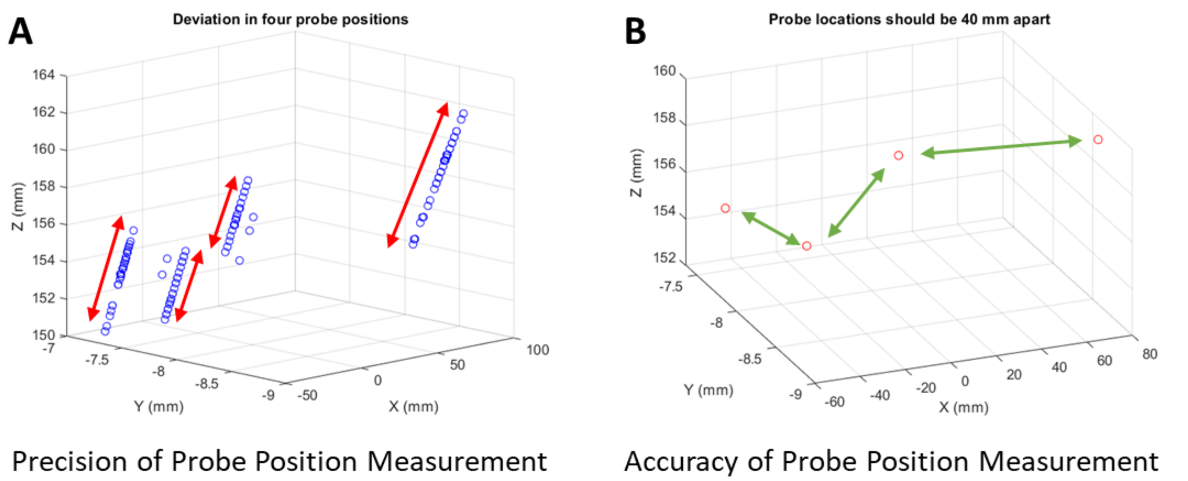

Figure 17. *Precision and accuracy experiment of the video-based stereo tracking of the probe.* ***A)*** *The red arrows depict the deviations in the probe position measurements. Where each of the four positions is measured for 60 frames.* ***B)*** *The green arrows depict the distance between the four probe positions, which should be 40mm. Here the four probe positions are the median of the distribution of locations shown in A.*

5.2.1 Results

Table 4 shows the accuracy of marker tracking versus stereoscopic tracking. A typical surgical operating distance from probe to endoscope is 100 mm. The stereoscopic has an accuracy of 4.0±2.7

mm versus an accuracy of 2.1±2.5 for marker tracking when the probe is at a depth of 90 to 130 mm. At a depth of 70 to 110 mm, stereoscopic tracking resulted in an accuracy of 1.4±0.6 mm versus 5.2±6.2.

However, looking at bigger distances from the endoscope, stereoscopic tracking is clearly more accurate than marker tracking. This difference might be largely explained by the lighting conditions at the in the images. Indeed, marker tracking is more prone to bad segmentation in this area because it uses the width in pixels of the segmented marker directly to calculate the depth of the probe. Figure 18 shows an example where this bad segmentation leads to an inaccurate depth estimation with marker tracking, while stereovision does not suffer from bad segmentation and results in a more robust tracking result in difficult lighting conditions.

	Marker tracking algorithm		**Stereo tracking algorithm**	
Depth (mm)	RMS±std (mm)	Std [x y z] (mm)	RMS±std (mm)	Std [x y z] (mm)
250-290	193.8±84	[14.6 7.1 73.3]	2.5±2.3	[2.3 4.3 13.5]
210-250	79.0±42.2	[9.6 7.0 58.0]	0.4±0.4	[1.2 0.6 6.7]
170-210	45.9±33.6	[4.8 3.9 24.0]	2.2±2.3	[0.8 0.7 5.4]
130-170	51.6±51.3	[4.4 1.0 9.3]	1.0±1.0	[0.5 0.1 1.3]
90-130	2.1±2.5	[1.4 0.3 2.4]	4.0±2.7	[2.3 0.2 4.3]
70-110	5.2±6.2	[0.3 0.3 0.9]	1.4±0.6	[2.8 0.7 4.8]

Table 4. *Results of marker tracking and stereo tracking accuracy. The RMS error is the error of the distance between measure points reported by the tracking software and the true distance (40 mm). The Std is the deviation in the x, y and z coordinate when the probe is stationary in 60 frames.*

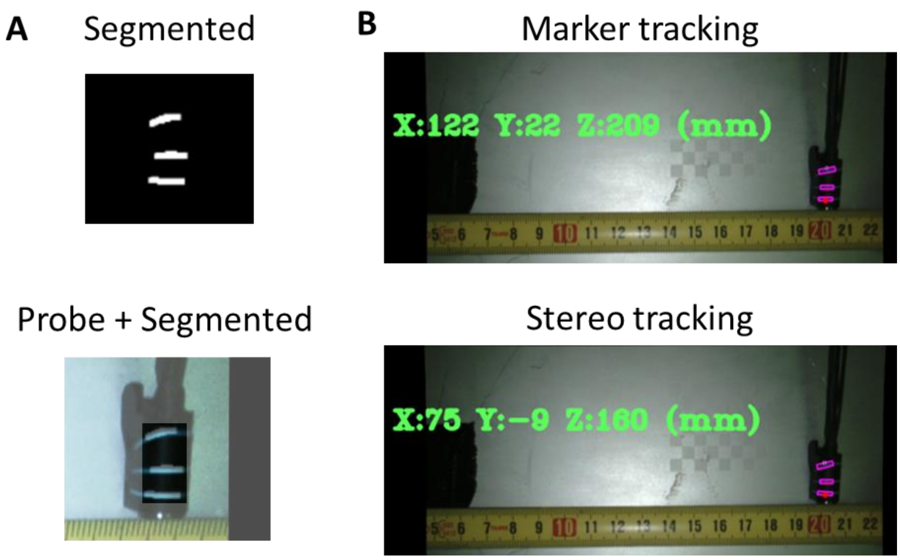

Figure 18. *Marker tracking vs Stereo tracking on 130-170 mm depth.* ***A)*** *Poorly segmented probe due to light conditions at the edge of the image.* ***B)*** *The result of Marker tracking and Stereo tracking. Due to the smaller segmented marker, marker tracking estimates the probe tip position deeper, whilst stereo tracker does not suffer this dependency on perfect segmentation.*

5.3 Accuracy IMU sensor

The angels that the IMU sensor must be able to record during surgery, can be divided into two groups (figure 19A): orientation int the xy-plane (the rotation by changing the robot arm), and orientation change around the z-axis (the rotation of the camera). To test these two cases, an experiment was performed where the IMU sensor was placed on an adjustable protractor. First horizontally (the change will be in the xy-plane) and secondly vertically placed on the rotation point (the change will include a change in yaw). The median angle before and after the change in orientation was recorded. Using the median angles of before and after the change, 3x3 rotation matrices were constructed. The distance in rotation between these two rotation matrices was recorded. The change in orientation was varied with 1, 5 and 10 degrees. For each of these three angles, the measurement was repeated 4 times.

To place the error in perspective, table 5 shows the impact of an error on the error introduced in the camera origin location, which affects the video-based DROP-IN tracking.

Error	Displacement
0.25 degrees	2.7 mm
0.5 degrees	5.4 mm
1 degree	10.8 mm
1.25 degrees	13.5 mm

Table 5. *Displacement error of the Firefly origin due to an angular error of the IMU sensor with 62cm between the IMU and Firefly endoscope.*

5.3.1 Results

Figure 19B shows the results of the IMU sensor accuracy experiment. The results of the experiment show that the IMU measurements are 0.6 ±0.1 degrees accurate with rotations from 1 to 10 degrees in the xy-plane and around the z-axis. The errors reported from the experiment result in a camera displacement of 5 to 10 mm.

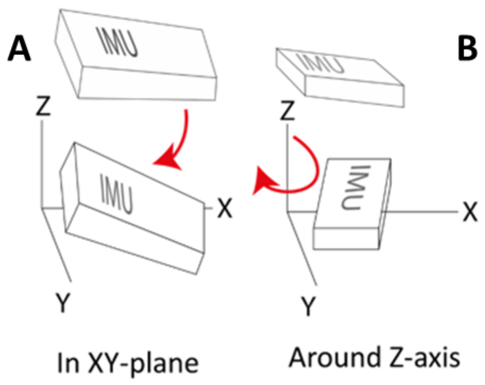

Rotation type	Degrees of change on protractor	IMU average error (std) in degrees
In xy-plane	1 degree	0.3839 (0.0981)
	5 degrees	0.5932 (0.1101)
	10 degrees	0.4625 (0.1167)
Around z-axis	1 degree	0.4162(0.1458)
	5 degrees	0.2623 (0.2055)
	10 degrees	0.5594 (0.1429)

Figure 19. *Results of the experiment for the IMU tracking accuracy.* ***A)*** *Schematic representation of the rotations of the IMU sensor during robotic surgery.* ***B)*** *Table listing the results of the IMU sensor accuracy and precision experiment of the two specified orientation changes during the robotic surgery.*

5.4 Registration algorithms performances

The research question if the SN location pattern can be used to register the preoperative to the intraoperative volume is crucial to the proposed method. For the image registration to be effective in clinical use, the algorithms will need to be able to deal with the errors in recording the intraoperative volume (introduced because of stereo tracking error, patient deformation, inaccuracy in pointing to the SN location). Moreover, often more SNs are found during surgery than identified on preoperative imaging. The registration algorithms will need to be able to deal with these extra removed SNs.

To test the registration algorithms, a simulation experiment was performed using clinical patient data. Using 13 patient SPECT/CT scans, the preoperative volume was extracted, and the intraoperative volume was simulated by introducing an error on the location.

5.4.1 Data simulation

Using reports from radiologists that identified the SNs in the patient SPECT/CT scans, the activity around of the SNs were segmented in RadiAnt™. To retrieve the preoperative locations of the SN's, the centre of the activity was calculated using the mean of the segmented locations. Patients that had less than 3 sentinel nodes were excluded from the dataset, because a minimal of 3 landmark locations is needed to find match the orientation of the scans.

5.4.2 Simulation experiment

The performance of the registration algorithms when all SNs were successfully removed. Random extra spots were generated around the existing intraoperative locations (random translation of x, y and z coordinate by [5-15] mm), to investigate if the registration algorithms could register the volumes correctly if more SNs are dissected than SNs imaged on the preoperative scans. The number of extra SNs ranged from 0 to 3. The locations in the preoperative volume were randomly translated to mimic error in recording the SN locations. These random errors were generated from normal distribution. Next, errors were introduced using 5 normal distributions with a mean error of 0mm and different variances (2mm, 5mm, 10mm, 15mm and 20 mm) to investigate the registration algorithms performances with increasing errors. The preoperative volume was randomly rotated (yaw, pitch, and roll range of [0-30] degrees) and translated (range of [-20,20] mm). After the generation of the preoperative and intraoperative SN locations, the three registration algorithms (ICP, CPD, Chamfer matching) were tested on the data set. After registering the preoperative volume to the intraoperative volume, the intraoperative locations were each assigned to the closest preoperative spot in the preoperative volume. If one of the preoperative SNs was not correctly linked to the intraoperative SN, the matching was considered a misclassification. The percentage of misclassifications in different error sizes was reported. The Euclidian distance between the paired pre- and intra-operative SN locations was calculated.

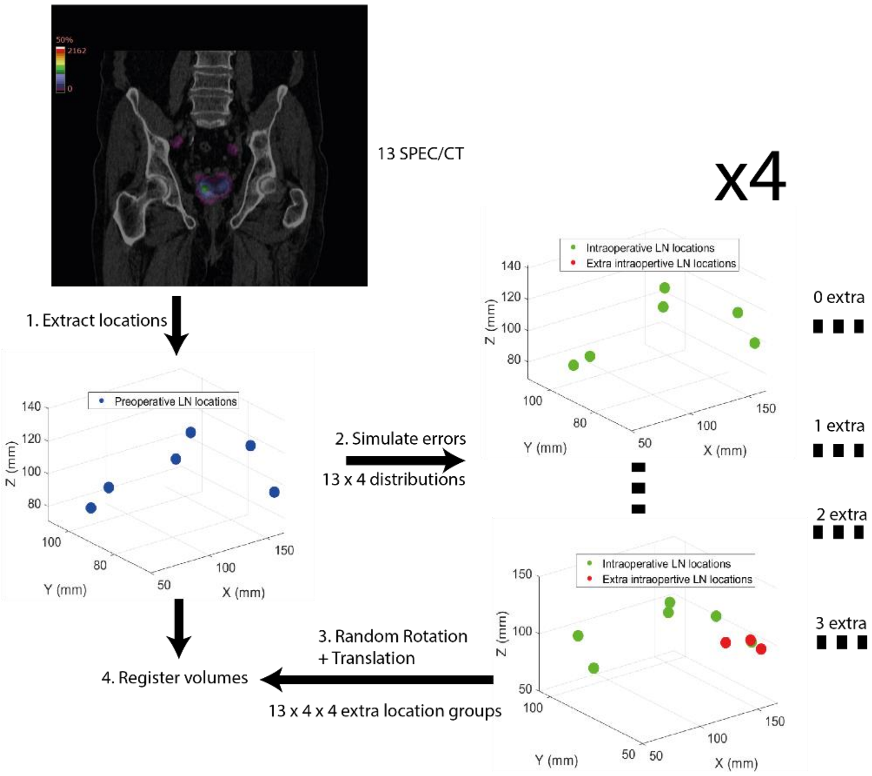

Figure 20. *Schematic overview of the simulation experiment. First the SN locations are extracted from the 13 patient SPECT/CT scans to make the preoperative volume. Next, the intraoperative volume is created by applying a random error on the preoperative volume locations. Four different error distributions are investigated. Next, extra LN are generated around existing locations, to simulate the removal of extra LNs during surgery. Then a random rotation and translation is applied, before the preoperative and simulated intraoperative volumes are registered using chamfer matching, ICP, and CPD.*

To depict the result of an error in the recording of the LN location, Appendix B lists the figures of the SN's from the 13 patient scans, where a sphere is drawn around the SN with the diameter of the 95-percentile range of the error applied in the simulation experiment. Figure 21 shows the difference between 2 patients, where for one patient a larger error results in a larger overlap in the 95-percentile range of expected errors. This overlap means that with perfect registration of the two volumes, due to an error in the intraoperative SN location, a mislabelling between the pre- and intra-operative location can occur. As there is now a possibility that the recorded SN location is closer to a neighbouring SN due to the error. The four 95-percintales used to construct the spheres for distribution 2mm, 5mm, 10mm and 15mm are: 5.7mm, 13.5mm, 29.6mm and 40.4mm. All patients have disjoint spheres with 2mm error distribution. Al patients except for patient 4 and 5, have disjoint spheres up to the 5mm error distribution. In the 10mm error distribution, only patient 3 has disjoint spheres. At the largest considered error distribution, no patient has disjointed spheres.

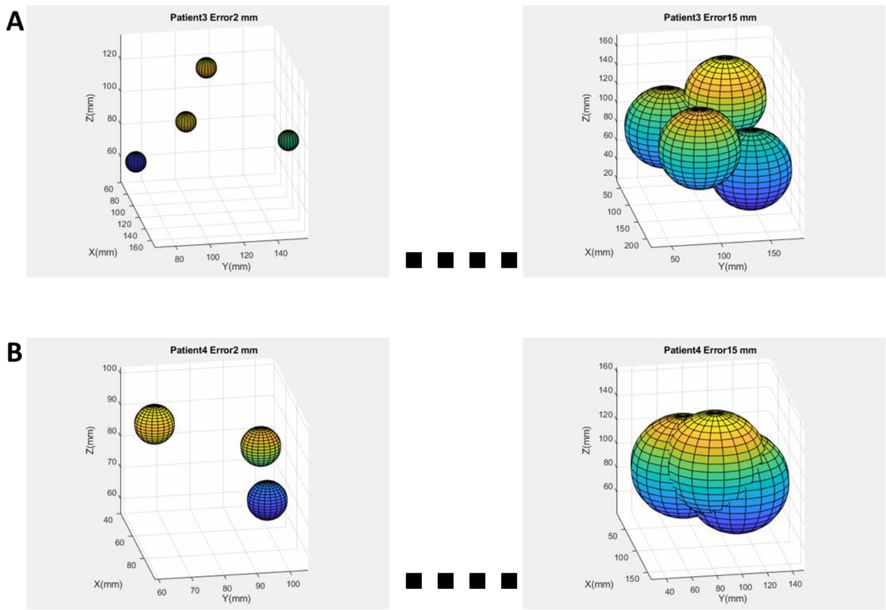

Figure 21. *Result of applying the 95-percentile of the error distribution (generated by normal distribution μ 0mm and σ 2mm and 15mm) on the SN locations from the SPECT scan.* ***A)*** *Patient 2 preoperative SN locations with 95 percentile error volumes (normal distribution σ 2mm and σ 15mm respectively).* ***B)*** *Patient 4 preoperative SN locations with 95 percentile error volumes (normal distribution σ 2mm and σ 15mm respectively).*

One challenge of the proposed method will be in the ability to deal with errors in the recorded intraoperative SN locations, due to the tracking setup or patient deformation. When the recorded intraoperative SN location SN_{e1} is closer to a neighbouring SN_n in the preoperative SN volume than the correct preoperative SN location SN_o, it is expected that the method results in an incorrect pairing of SN_e to SN_n. We can express the ratio of the distance of the intraoperative SN_e to its corresponding preoperative locations SN_o over the distance of SN_e to the closest neighbouring preoperative SN location SN_n other than SN_o. We expect that if the specified ratio is over 1, the distance between our simulated intraoperative SN_{e1} locations and a neighbouring SN_n is smaller than the distance to the 'original' SN_o. This leads to an incorrect pairing of the intraoperative SN_e to the neighbouring SN_n. If the ratio is smaller than 1, the distance to the 'original' SN_o is smaller than the distance to any neighbouring SN_n, so the intraoperative SN will be correctly assigned to the 'original' SN_o. The purpose of this ratio is to show that if the registration algorithms can perfectly undo the introduced random rotation and translation, the described cut-off at 1 will hold. The max error ratio could give insight in up to what error the registration algorithms result in a correct pairing of SN locations.

Statistical significance was established with the paired t-test with critical p-value $\alpha=0.05$, to compare the performance on the different extra SNs and between the registration algorithms. To correct for testing on the same dataset multiple times, the Bonferroni correction was used (α/number of comparisons).

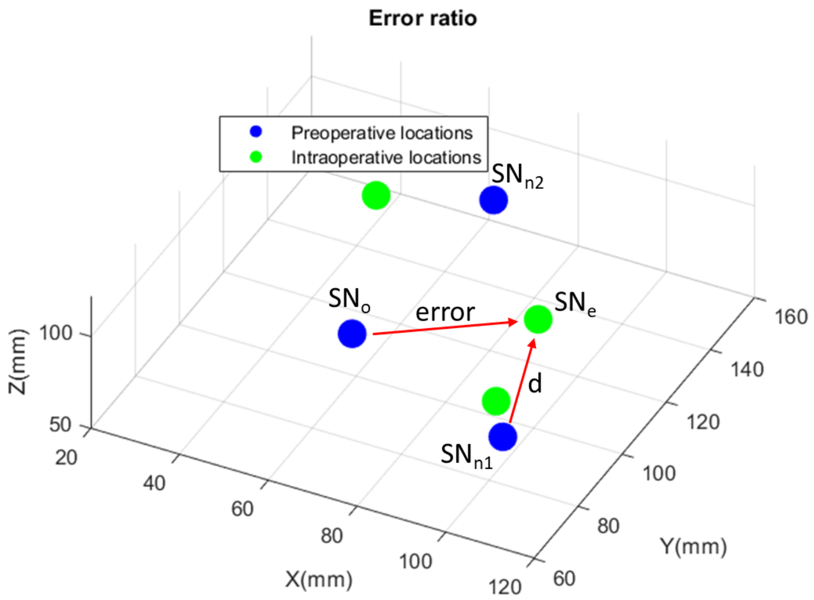

Figure 22. *Example of a calculation of the error ratio (error/d) of* SN_e.

5.4.3 Results

Table 6 presents the performance of the three registration algorithms tested with different errors in the intraoperative location volume. The registration algorithms do not show to differ in the first two error groups. Chamfer matching results in the best accuracy in the third error group, while the ICP algorithm has the highest accuracy in the last and biggest error group. No evidence was found that that the extra LNs influenced the registration algorithm performance. Table 7 in Appendix C shows no significant difference between the registration results when the number of extra LNs is varied. Table 8 reports the distances between the intraoperative and preoperative SN locations after registration for the three algorithms. These results suggest that chamfer matching (group 1, 2 and 3) and ICP (group 2 and 4) both achieve significant lower RMS distances after registration than CPD. the distance between the SN locations in the intraoperative and preoperative volume than CPD. ICP achieves significantly lower distances than chamfer matching in group 4.

Data			ICP	CPD	Chamfer matching
Error group	**Avg. max error (mm)**	**Avg. error (mm)**	**Pairing Accuracy**	**Pairing Accuracy**	**Pairing Accuracy**
1	4.7±0.9	3.1 ±1.3	98%	**100%**	**100%**
2	11.7±2.6	7.8 ±3.2	**100%**	98%	**100%**
3	23.5±5.4	15.6 ±6.6	73%	75%	**81%**
4	35.0±6.7	23.6 ±9.3	**67%**	50%	54%

Table 6. *Results from simulation experiment. Per error group, the average of the maximal error introduced in the patient scan is listed, the average within the group of the average error introduced in the patient scans. For the three tested registration algorithms, the percentage of cases where all intraoperative SNs were correctly paired with preoperative SN locations.*

Data		ICP	CPD		Chamfer matching		
Error group	**N=**	**Avg. dist. (mm)**	**Avg. rms. (mm)**	**P value t-test vs ICP**	**Avg. dist. (mm)**	**P value t-test vs ICP**	**P value t-test vs CPD**
1	52	3.0 ±2.7	2.5±1.4	0.2602	2.6±1.1	0.2953	**0.0014**
2	52	6.7±2.4	8.1±3.0	**<0.001**	6.4±1.8	0.1163	**<0.001**
3	52	15.8±7.4	17.6±6.1	0.0571	14.2±5.9	0.1339	**<0.001**
4	52	21.7±8.0	27.3±10.8	**<0.001**	24.5±12.4	**0.0169**	0.0755

Table 8. *Paired t-test results between the registration algorithms with α=0.025 after Bonferroni correction, showing statistical significance in the ability to minimise the distance between the preoperative and intraoperative SN locations. The average of the RMS for all cases that resulted from the registration varying the error size on the intraoperative volume is reported.*

Figure 23 shows the results of the error ratio in the four different simulated error groups. In the last two error groups, the registration of the preoperative and intraoperative SN location volumes starts resulting in incorrect pairings when this ratio is over 0.5.

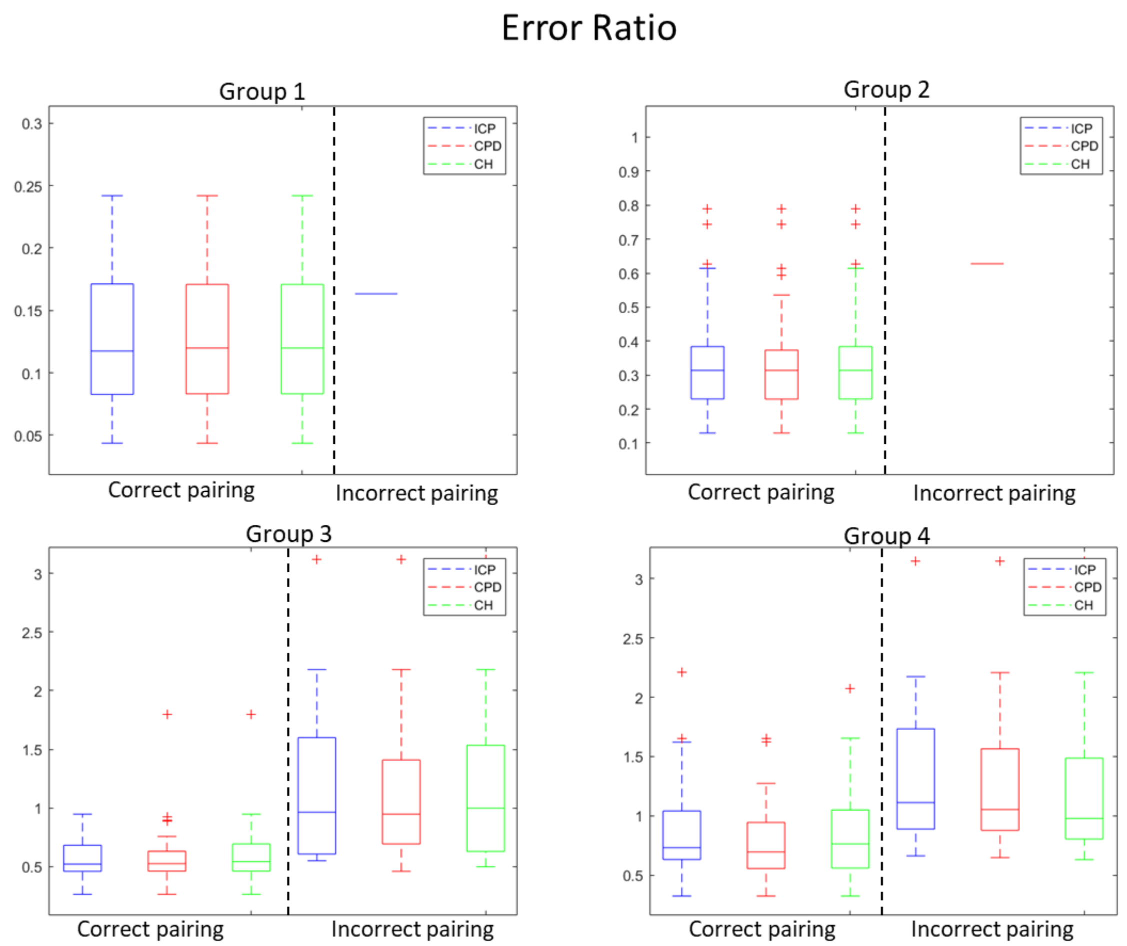

Figure 23. *The max ratio in the patient scans of the distance between the intraoperative SN location and the correct preoperative SN location over the distance between the intraoperative SN and the closest neighbouring preoperative SN location. For the three registration algorithms, the data is split in two groups where the correct pairing group contains the max ratio in the cases that resulted in a correct pairing of SN locations, and the incorrect pairing contains the max ratio in the cases that resulted in one or more incorrect pairing of SN locations.*

Chapter 6
Discussion and conclusion

6.1 Discussion and future work

Currently, a discordance between the preoperative and intraoperative SN location findings exists. The challenge of this study was to develop a robust method that can link the preoperative and intraoperative SN locations, and which could be translated into clinical practise down the line. To this end, this thesis proposed a method that introduced a robust video-based stereo tracking solution to record the pattern of SNs during the robotic SN procedure, such that the pattern could be used to match preoperative and intraoperative SN locations. From the video-based tracking accuracy experiment, the video-based stereo tracking had an accuracy of 4.0±2.7mm and showed to be more robust than marker tracking. This is due to the smaller dependency on the segmentation of the markers. Segmenting the probe during surgery is a challenging task, as light conditions will vary greatly. The setting for the threshold to extract the markers from the video will therefore influence the accuracy of the marker-based tracking algorithm. By exploiting the stereo principle, the depth is found by comparing the left and right images, and accuracy in approximating the depth of the probe is no longer depended on the width of the segmented marker. The marker is only used to recognise the DROP-IN probe in the video and used to find the middle of the probe. Video-based stereo tracking results in a more generalised and robust solution for tracking the DROP-IN probe with markers during surgery.

A first step in a routine friendly endoscope tracking technique with the IMU sensor was done. Tracking of the endoscope was previously accomplished using near-infra red tracking [8, 10]. Tracking the endoscope with near infra-red during routine surgery is however complicated, due to the added complexity because of the line-of-sight issue and having to sterilise the tracking fiducials that need to be placed outside the sterile covers. The IMU sensor tracking can be placed on top of the endoscope under the sterile cover and could be read out using a wireless connection, which makes it a much friendlier solutions to capture the endoscope orientations. The IMU sensor was shown to be able to capture the endoscopic rotations and can be used to record the orientations of the Firefly camera with an accuracy of 0.6±0.15 degrees. Although IMU tracking was sufficient to record the rotations of the Firefly endoscope, no automatic measurement for the insertion distance from the IMU to the trocar was yet implemented. Further research is needed to find a reliable method to measure the distance between the IMU sensor and the trocar. The IMU sensor itself could be used to measure the zoom of the endoscope into the patient. A drawback is the drift of the IMU sensor that introduces error due to the double integration over the measured acceleration. Another viable solution could be to extend the IMU solution with a near infra-red laser sensor, which measures the distance of the camera to a fixed point (such as the trocar).

The experiment that used clinical patient data to extract the preoperative SN location volume and simulated the intraoperative SN location volume showed that the registration algorithms could pair the preoperative volume to the intraoperative volume using only the pattern of the SNs as reference. No evidence of an influence of extra intraoperative SNs on the registration of the volumes was found. Chamfer matching was able to achieve significant lower RMS distances between preoperative and the corresponding intraoperative LN locations than CPD until an error of 15.6±6.6mm. Interestingly, also ICP achieved significant lower RMS, and even lower than Chamfer matching in the biggest error group, despite being known for being prone to outliers. Furthermore, the simulation results suggest that when the ratio of error over closest neighbouring SN location after error exceeds 0.5, incorrect pairings of preoperative and intraoperative SN locations start to occur. This would mean that if two SN locations are at 30mm, an error above 10mm in recording the intraoperative SN locations could result in an incorrect pairing of the recorded intraoperative SN and its corresponding preoperative SN in the scan. Further research with more data is needed to confirm this finding.

A limitation of the method is that the current method can only analyse patients with 3 or more imaged SNs. To adjust the method to deal with patients with less than 3 SNs, more landmarks need to be added to the pattern of SNs. Finding other viable landmarks could prove to be difficult due to the issue of deformations of soft tissue, however a 2021 study showed in animal models that pelvic arteries experience minor deformations (<2.1 mm) during laparoscopic surgery [47]. The arteries could be segmented out the CT scan, and the surgical video and added to the volumes as added landmarks. This would increase the potency of the method by increasing the error ratio threshold.

To further extend the proposed method, the counts of the DROP-IN probe itself could be included to improve the recording of the physical location of a SN during surgery by using the counts to scan for the SN location. The counts of the DROP-IN probe could also aid in differentiating between SNs and higher echelons (SNs should have higher tracer counts than higher echelon nodes). Next, to quantify the accuracy of the method, the propagation of the errors introduced by the tracking, registration and deformation of the patient needs to be researched. For now, the errors in the simulation experiment were simulated using a normal distributed error over the three coordinates. A different approach would be to simulate the error over the sphere that the error forms around the SN location. Ultimately, the goal would be to implement the method in routine clinical procedures. To reach this stage, the tracking of the Firefly must be able record besides the rotation, the translation of the camera as well. When clinical patient data is being recorded, the impact of patient deformation on the preoperative and intraoperative volume registration could be investigated.

This thesis researched the method in the context of the SN procedure in prostate cancer. The same method could ultimately be applied to PSMA guided LN dissection. This procedure aims to remove LNs that specifically contain tumour. The DROP-IN is used to detect tracer signal, which marks tumour positive LNs [48-51].

6.2 Concluding remarks

In conclusion, it was shown that stereoscopic probe tracking provides a robust probe tracking solution. IMU tracking can be used to track the orientation of the Firefly, without adding more complexity the OR. Using the proposed tracking setup in a phantom setting, the intraoperative SN pattern was successfully recorded and matched with the preoperative locations. Registration algorithms show promise in their ability to register the preoperative and intraoperative SN volume such that the SN locations can be paired.

References

1. Ficarra, V., et al., *Systematic review and meta-analysis of studies reporting potency rates after robot-assisted radical prostatectomy.* European urology, 2012. **62**(3): p. 418-430.
2. Dell'Oglio, P., et al., *A DROP-IN gamma probe for robot-assisted radioguided surgery of lymph nodes during radical prostatectomy.* European Urology, 2021. **79**(1): p. 124-132.
3. Briganti, A., et al., *Complications and other surgical outcomes associated with extended pelvic lymphadenectomy in men with localized prostate cancer.* European urology, 2006. **50**(5): p. 1006-1013.
4. Briganti, A., et al., *Pelvic lymph node dissection in prostate cancer.* European urology, 2009. **55**(6): p. 1251-1265.
5. Grivas, N., et al., *The impact of adding sentinel node biopsy to extended pelvic lymph node dissection on biochemical recurrence in prostate cancer patients treated with robot-assisted radical prostatectomy.* Journal of Nuclear Medicine, 2018. **59**(2): p. 204-209.
6. Mazzone, E., et al., *Diagnostic Value, Oncologic Outcomes, and Safety Profile of Image-Guided Surgery Technologies During Robot-Assisted Lymph Node Dissection with Sentinel Node Biopsy for Prostate Cancer.* Journal of Nuclear Medicine, 2021. **62**(10): p. 1363-1371.
7. van Oosterom, M.N., et al., *Computer-assisted surgery: virtual-and augmented-reality displays for navigation during urological interventions.* Current opinion in urology, 2018. **28**(2): p. 205-213.
8. Brouwer, O.R., et al., *Feasibility of intraoperative navigation to the sentinel node in the groin using preoperatively acquired single photon emission computerized tomography data: transferring functional imaging to the operating room.* The Journal of urology, 2014. **192**(6): p. 1810-1816.
9. Banz, V.M., et al., *Intraoperative image-guided navigation system: development and applicability in 65 patients undergoing liver surgery.* Langenbeck's archives of surgery, 2016. **401**(4): p. 495-502.
10. van Oosterom, M.N., et al., *Navigation of fluorescence cameras during soft tissue surgery—is it possible to use a single navigation setup for various open and laparoscopic urological surgery applications?* The Journal of Urology, 2018. **199**(4): p. 1061-1068.
11. Hawkes, D.J., et al., *Tissue deformation and shape models in image-guided interventions: a discussion paper.* Medical Image Analysis, 2005. **9**(2): p. 163-175.
12. Waelkens, P., et al., *Surgical navigation: an overview of the state-of-the-art clinical applications.* Radioguided Surgery, 2016: p. 57-73.
13. Altamar, H.O., et al., *Kidney deformation and intraprocedural registration: a study of elements of image-guided kidney surgery.* Journal of endourology, 2011. **25**(3): p. 511-517.
14. Dumpuri, P., et al., *Model-updated image-guided liver surgery: preliminary results using surface characterization.* Progress in biophysics and molecular biology, 2010. **103**(2-3): p. 197-207.
15. Baeten, I.G., et al., *Feasibility of a drop-in γ-probe for radioguided sentinel lymph detection in early-stage cervical cancer.* EJNMMI research, 2022. **12**(1): p. 1-8.
16. Meershoek, P., et al., *Robot-assisted laparoscopic surgery using DROP-IN radioguidance: first-in-human translation.* European journal of nuclear medicine and molecular imaging, 2019. **46**(1): p. 49-53.
17. van Oosterom, M.N., et al., *Revolutionizing (robot-assisted) laparoscopic gamma tracing using a drop-in gamma probe technology.* American journal of nuclear medicine and molecular imaging, 2016. **6**(1): p. 1.
18. JM, A.J., et al., *Sentinel Lymph Node Biopsy in Prostate Cancer Using the SENSEI® Drop-In Gamma Probe.* Clinical Nuclear Medicine, 2021.

19. Vorbeck, F., et al., *Intraoperative Navigation in der Nasennebenhöhlenchirurgie mit dem Philips „Neuroguide"-System.* Der Radiologe, 2000. **40**(3): p. 227-232.
20. Azargoshasb, S., et al., *Optical Navigation of the Drop-In γ-Probe as a Means to Strengthen the Connection Between Robot-Assisted and Radioguided Surgery.* Journal of Nuclear Medicine, 2021. **62**(9): p. 1314-1317.
21. Poulin, F. and L.-P. Amiot, *Interference during the use of an electromagnetic tracking system under OR conditions.* Journal of biomechanics, 2002. **35**(6): p. 733-737.
22. Sadjadi, H., K. Hashtrudi-Zaad, and G. Fichtinger, *Simultaneous electromagnetic tracking and calibration for dynamic field distortion compensation.* IEEE Transactions on Biomedical Engineering, 2015. **63**(8): p. 1771-1781.
23. Andria, G., et al., *Development and performance evaluation of an electromagnetic tracking system for surgery navigation.* Measurement, 2019. **148**: p. 106916.
24. Kumar, S., et al. *Product of tracking experts for visual tracking of surgical tools*. in *2013 IEEE International Conference on Automation Science and Engineering (CASE)*. 2013. IEEE.
25. Übelhör, T., et al., *3D camera-based markerless navigation system for robotic osteotomies.* at-Automatisierungstechnik, 2020. **68**(10): p. 863-879.
26. Hao, R., O. Özgüner, and M.C. Çavuşoğlu. *Vision-based surgical tool pose estimation for the da vinci® robotic surgical system*. in *2018 IEEE/RSJ international conference on intelligent robots and systems (IROS)*. 2018. IEEE.
27. Rieke, N., et al. *Surgical tool tracking and pose estimation in retinal microsurgery*. in *International Conference on Medical Image Computing and Computer-Assisted Intervention*. 2015. Springer.
28. Richa, R., et al. *Visual tracking of surgical tools for proximity detection in retinal surgery*. in *International Conference on Information Processing in Computer-Assisted Interventions*. 2011. Springer.
29. El-Haddad, M.T. and Y.K. Tao, *Automated stereo vision instrument tracking for intraoperative OCT guided anterior segment ophthalmic surgical maneuvers.* Biomedical optics express, 2015. **6**(8): p. 3014-3031.
30. Allan, M., et al., *Stereo correspondence and reconstruction of endoscopic data challenge.* arXiv preprint arXiv:2101.01133, 2021.
31. Hirschmuller, H., *Stereo processing by semiglobal matching and mutual information.* IEEE Transactions on pattern analysis and machine intelligence, 2007. **30**(2): p. 328-341.
32. Birchfield, S. and C. Tomasi, *A pixel dissimilarity measure that is insensitive to image sampling.* IEEE Transactions on Pattern Analysis and Machine Intelligence, 1998. **20**(4): p. 401-406.
33. Besl, P.J. and N.D. McKay. *Method for registration of 3-D shapes*. in *Sensor fusion IV: control paradigms and data structures*. 1992. Spie.
34. Sorkine, O., *Least-squares rigid motion using svd.* Technical notes, 2009. **120**(3): p. 52.
35. Borgefors, G., *Hierarchical chamfer matching: A parametric edge matching algorithm.* IEEE Transactions on pattern analysis and machine intelligence, 1988. **10**(6): p. 849-865.
36. Myronenko, A. and X. Song, *Point set registration: Coherent point drift.* IEEE transactions on pattern analysis and machine intelligence, 2010. **32**(12): p. 2262-2275.
37. Van Herk, M., et al., *Effect of image artifacts, organ motion, and poor segmentation on the reliability and accuracy of three-dimensional chamfer matching.* Computer Aided Surgery: Official Journal of the International Society for Computer Aided Surgery (ISCAS), 1997. **2**(6): p. 346-355.
38. Zhang, X., et al., *A markerless automatic deformable registration framework for augmented reality navigation of laparoscopy partial nephrectomy.* International Journal of Computer Assisted Radiology and Surgery, 2019. **14**(8): p. 1285-1294.

39. Jiang, H., K.S. Holton, and R.A. Robb. *Image registration of multimodality 3D medical images by chamfer matching*. in *Biomedical Image Processing and Three-Dimensional Microscopy*. 1992. SPIE.
40. Thiran, J.-P., B. Macq, and C. Michel. *Morphological registration of 3D medical images*. in *Proceedings of 3rd IEEE International Conference on Image Processing*. 1996. IEEE.
41. Cai, J., et al., *CT and PET lung image registration and fusion in radiotherapy treatment planning using the chamfer-matching method.* International Journal of Radiation Oncology* Biology* Physics, 1999. **43**(4): p. 883-891.
42. Bradski, G., *The openCV library.* Dr. Dobb's Journal: Software Tools for the Professional Programmer, 2000. **25**(11): p. 120-123.
43. Madgwick, S.O., *AHRS algorithms and calibration solutions to facilitate new applications using low-cost MEMS*. 2014, University of Bristol.
44. Azargoshasb, S., et al., *The Click-On gamma probe, a second-generation tethered robotic gamma probe that improves dexterity and surgical decision-making.* European Journal of Nuclear Medicine and Molecular Imaging, 2021. **48**(13): p. 4142-4151.
45. Vinnicombe, S.J., et al., *Normal pelvic lymph nodes: evaluation with CT after bipedal lymphangiography.* Radiology, 1995. **194**(2): p. 349-355.
46. Zhang, Z., *A flexible new technique for camera calibration.* IEEE Transactions on pattern analysis and machine intelligence, 2000. **22**(11): p. 1330-1334.
47. Kiyomatsu, H., et al., *Deformation of the pelvic arteries caused by pneumoperitoneum and postural changes in an animal model.* in vivo, 2021. **35**(1): p. 275-281.
48. de Barros, H.A., et al., *Robot-assisted Prostate-specific Membrane Antigen–radioguided Salvage Surgery in Recurrent Prostate Cancer Using a DROP-IN Gamma Probe: The First Prospective Feasibility Study.* European Urology, 2022.
49. De Barros, H., et al., *Minimally invasive robot-assisted PSMA-guided salvage surgery in recurrent prostate cancer using DROP-IN radioguidance*. 2021, Soc Nuclear Med.
50. Gondoputro, W., et al., *Robot-assisted prostate-specific membrane antigen-radioguided surgery in primary diagnosed prostate cancer.* Journal of Nuclear Medicine, 2022.
51. Gandaglia, G., et al., *Prostate-specific membrane antigen radioguided surgery to detect nodal metastases in primary prostate cancer patients undergoing robot-assisted radical prostatectomy and extended pelvic lymph node dissection: Results of a planned interim analysis of a prospective phase 2 study.* European Urology, 2022. **82**(4): p. 411-418.

Appendix A

Baseline translation [x y z]: -4.3014683359121166e+00 0. 0

Baseline rotation (3x3):

9.9999889817438115e-01 6.9786956762589577e-05 -1.4828283124567402e-03

-6.7762527451174065e-05 9.9999906574306940e-01 1.3652550048496655e-03

1.4829222041061075e-03 -1.3651530203824948e-03 9.9999796864742052e-01

Intrinsic camera calibration matrix (3x3):

1.0706188663934486e+03 0. 9.3580034306269090e+02

0. 1.0715737551305006e+03 5.0638640756917050e+02

0. 0. 1.

SGBM

This algorithm uses multiple parameters to find the disparity map. In this thesis, the impact of different parameter settings on the accuracy of the disparity map has not been investigated. The following parameters and their settings were used during this thesis project:

Min disparity: 0

Number of disparities: 18*16

Prefilter cap: Filtering before SGBM 20

Speckle Range: Specifies the maximal distance between pixels that form a blob: 0

Speckle Window Size: Blobs lower than this size get removed from the disparity map: 0

Uniqueness ratio: Threshold for dissimilarity function, pixel scoring lower than 15 are not matched 15

P1: The penalty for 1 disparity lower than the neighbouring disparity 8*channels * $wsize^2$

P2: The penalty for more than 1 disparity lower than the neighbouring disparity 36*channels * $wsize^2$

Appendix B

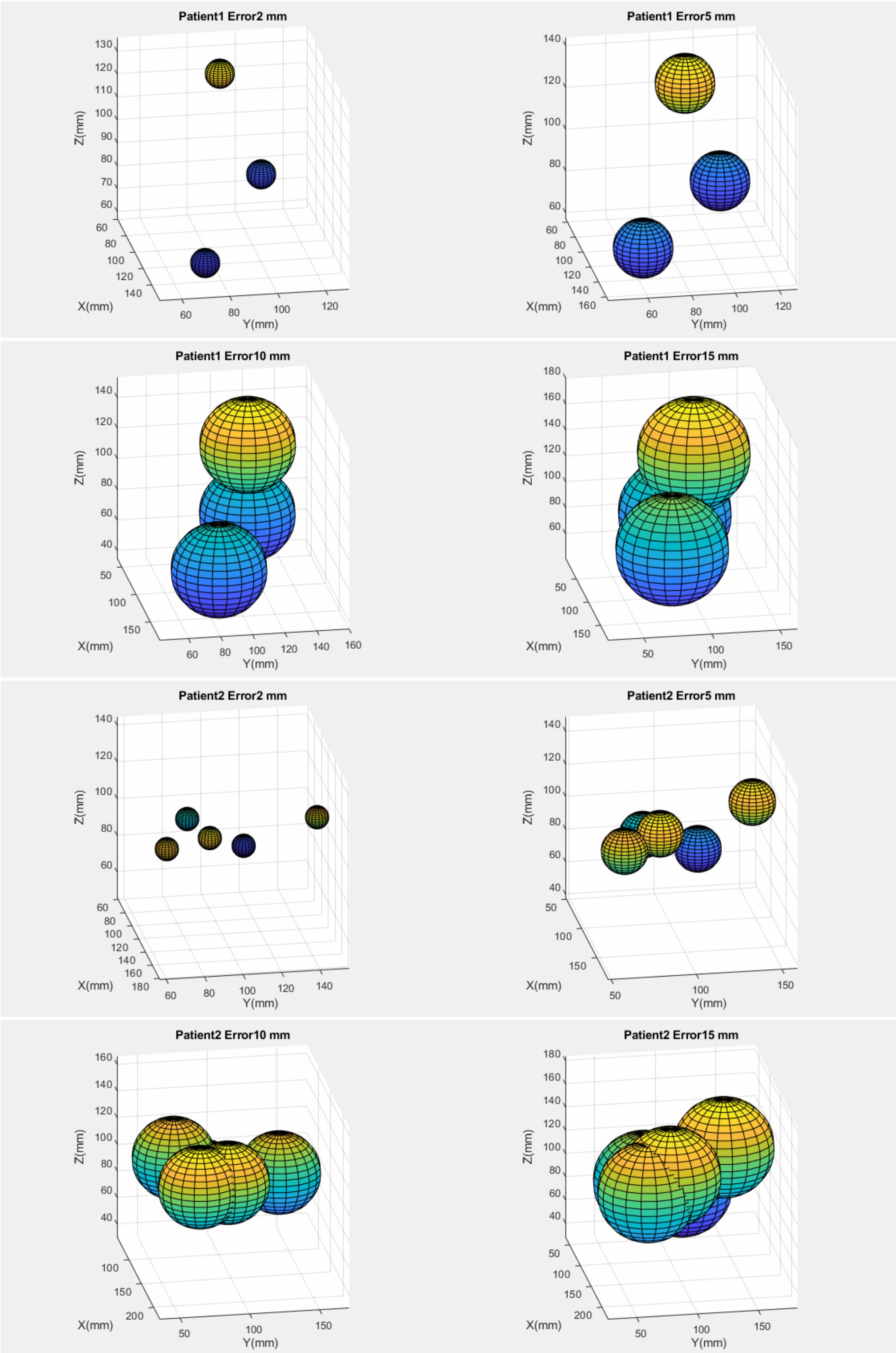

Patient1 Error2 mm
Patient1 Error5 mm
Patient1 Error10 mm
Patient1 Error15 mm
Patient2 Error2 mm
Patient2 Error5 mm
Patient2 Error10 mm
Patient2 Error15 mm
X(mm)
Y(mm)
Z(mm)

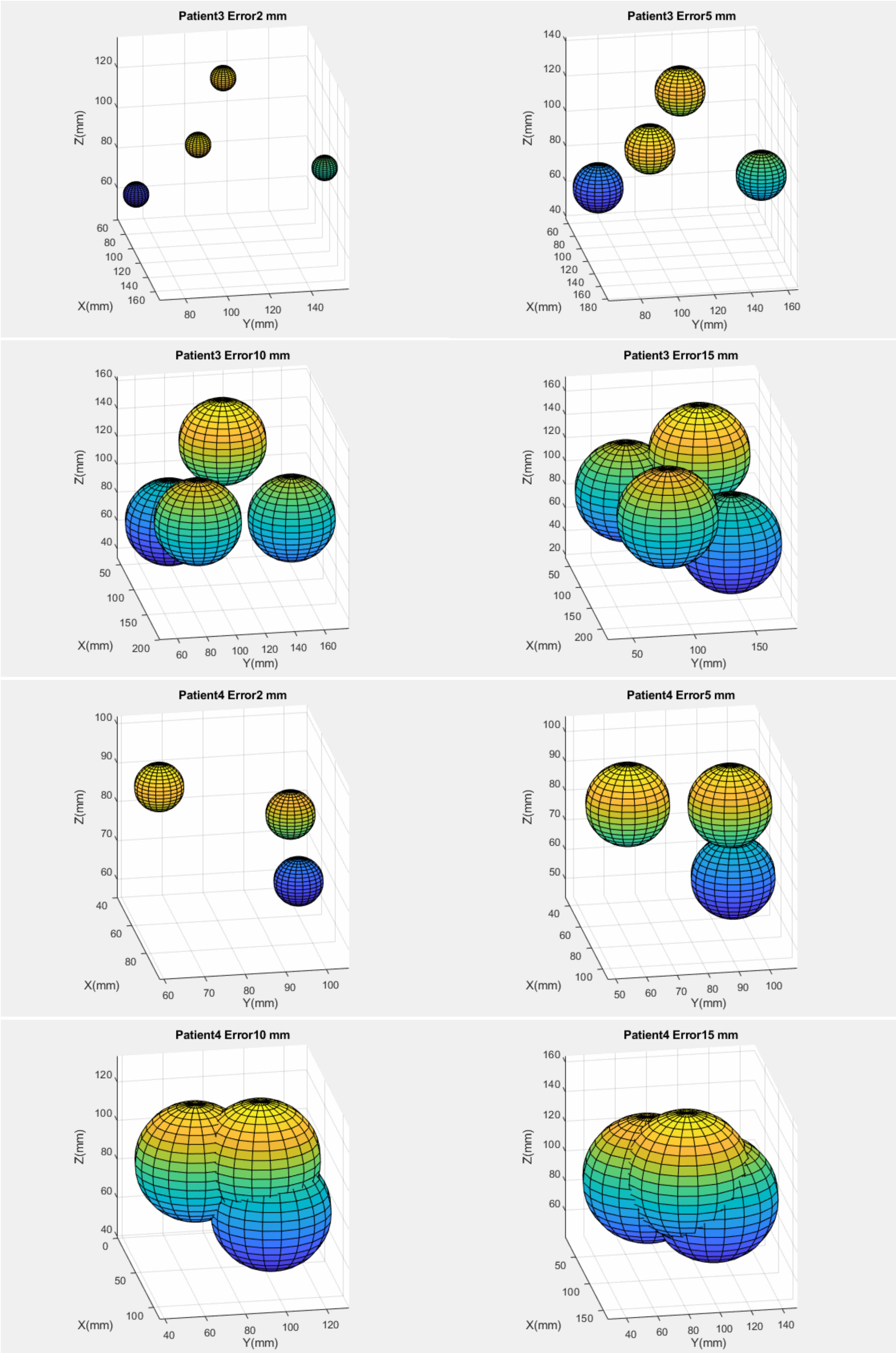
Patient3 Error2 mm
Patient3 Error5 mm
Patient3 Error10 mm
Patient3 Error15 mm
Patient4 Error2 mm
Patient4 Error5 mm
Patient4 Error10 mm
Patient4 Error15 mm
Z(mm)
X(mm)
Y(mm)

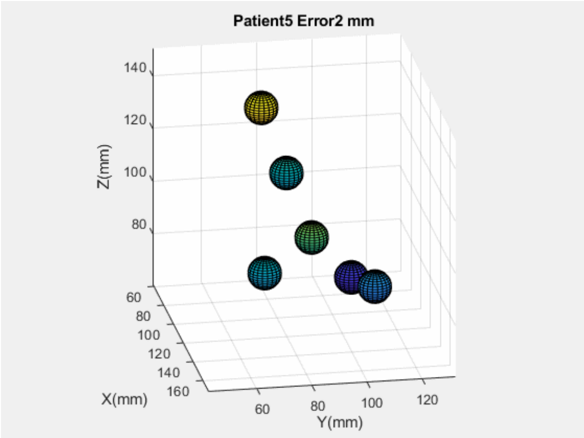
Patient5 Error2 mm
Z(mm)
X(mm)
Y(mm)

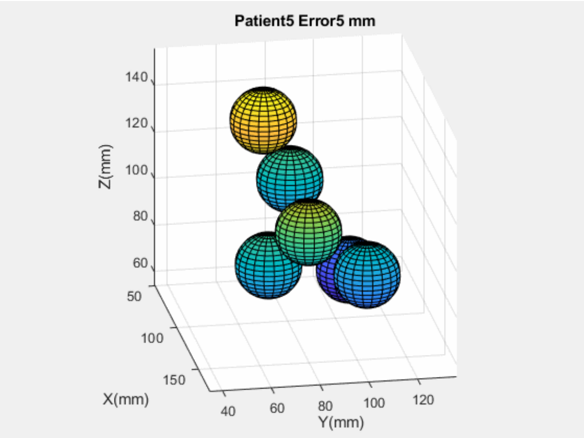
Patient5 Error5 mm
Z(mm)
X(mm)
Y(mm)

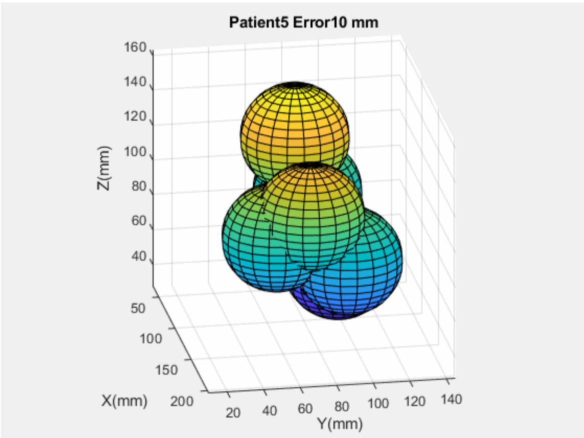
Patient5 Error10 mm
Z(mm)
X(mm)
Y(mm)

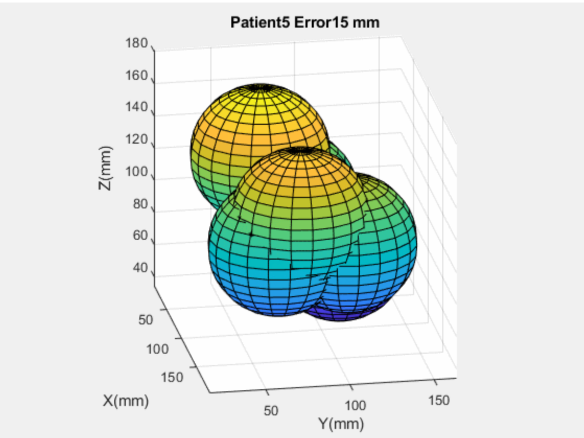
Patient5 Error15 mm
Z(mm)
X(mm)
Y(mm)

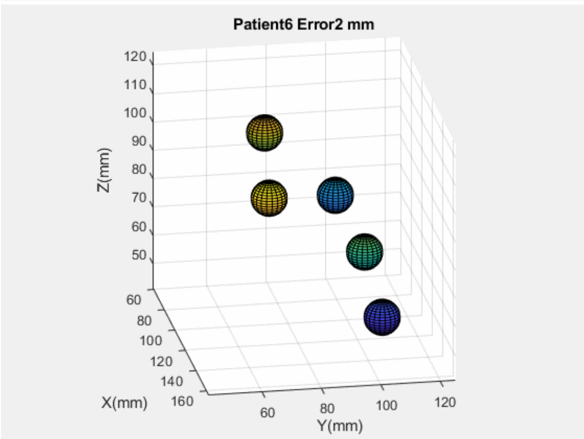
Patient6 Error2 mm
Z(mm)
X(mm)
Y(mm)

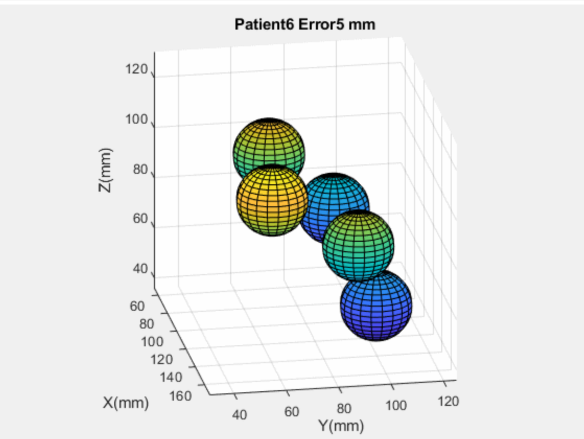
Patient6 Error5 mm
Z(mm)
X(mm)
Y(mm)

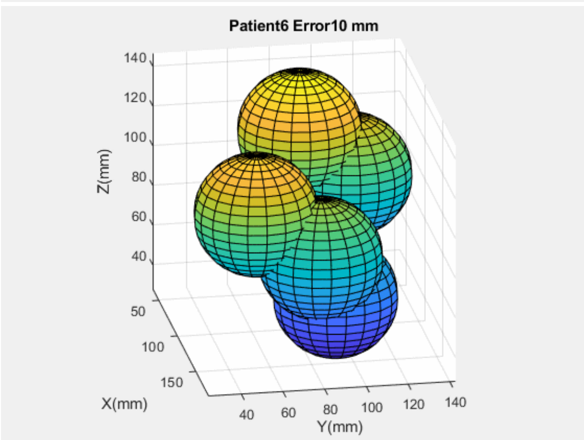
Patient6 Error10 mm
Z(mm)
X(mm)
Y(mm)

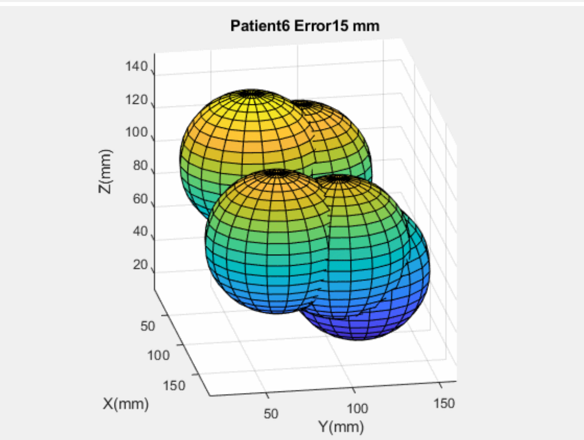
Patient6 Error15 mm
Z(mm)
X(mm)
Y(mm)

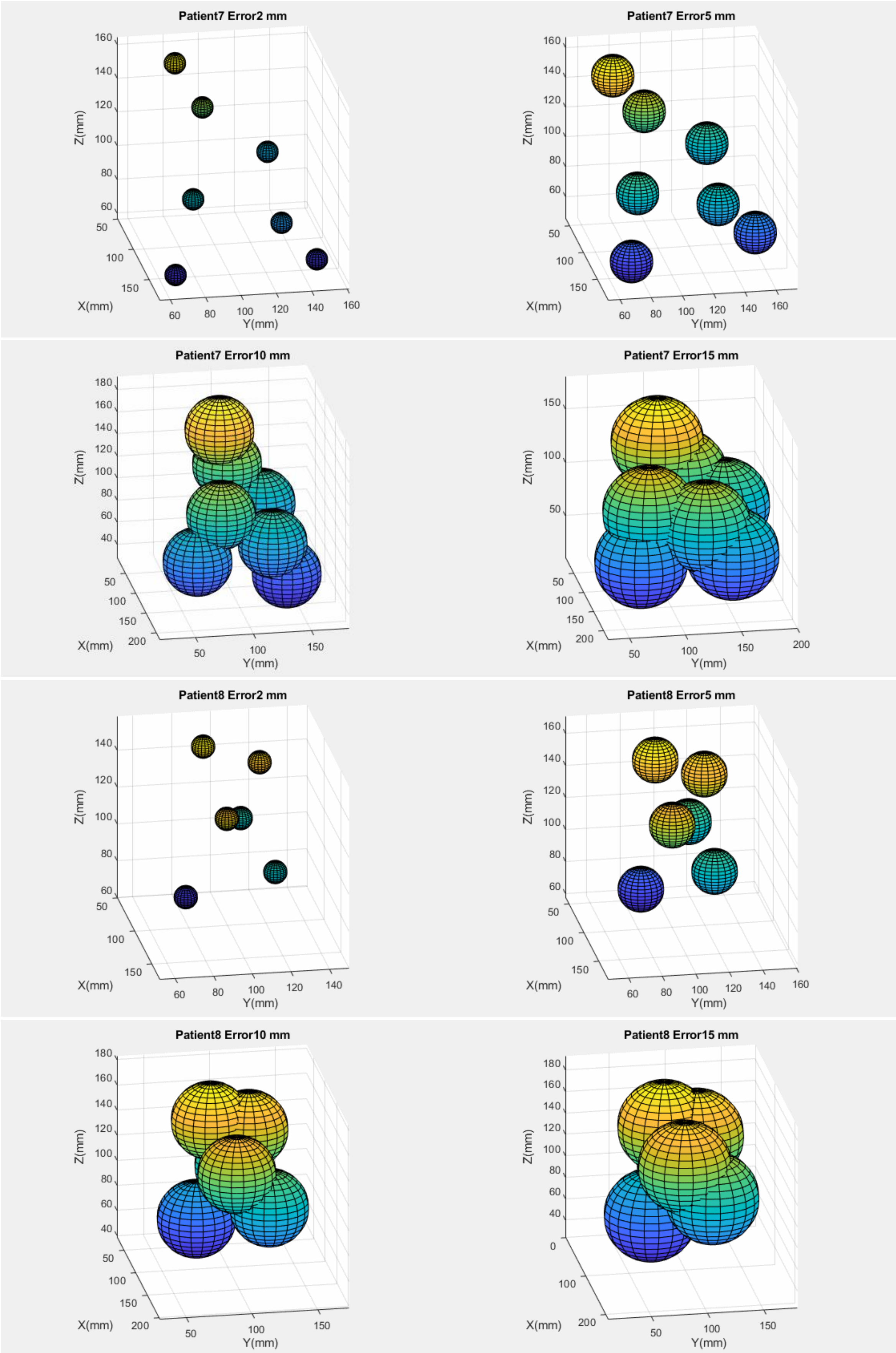
Patient7 Error2 mm
Patient7 Error5 mm
Patient7 Error10 mm
Patient7 Error15 mm
Patient8 Error2 mm
Patient8 Error5 mm
Patient8 Error10 mm
Patient8 Error15 mm
Z(mm)
X(mm)
Y(mm)

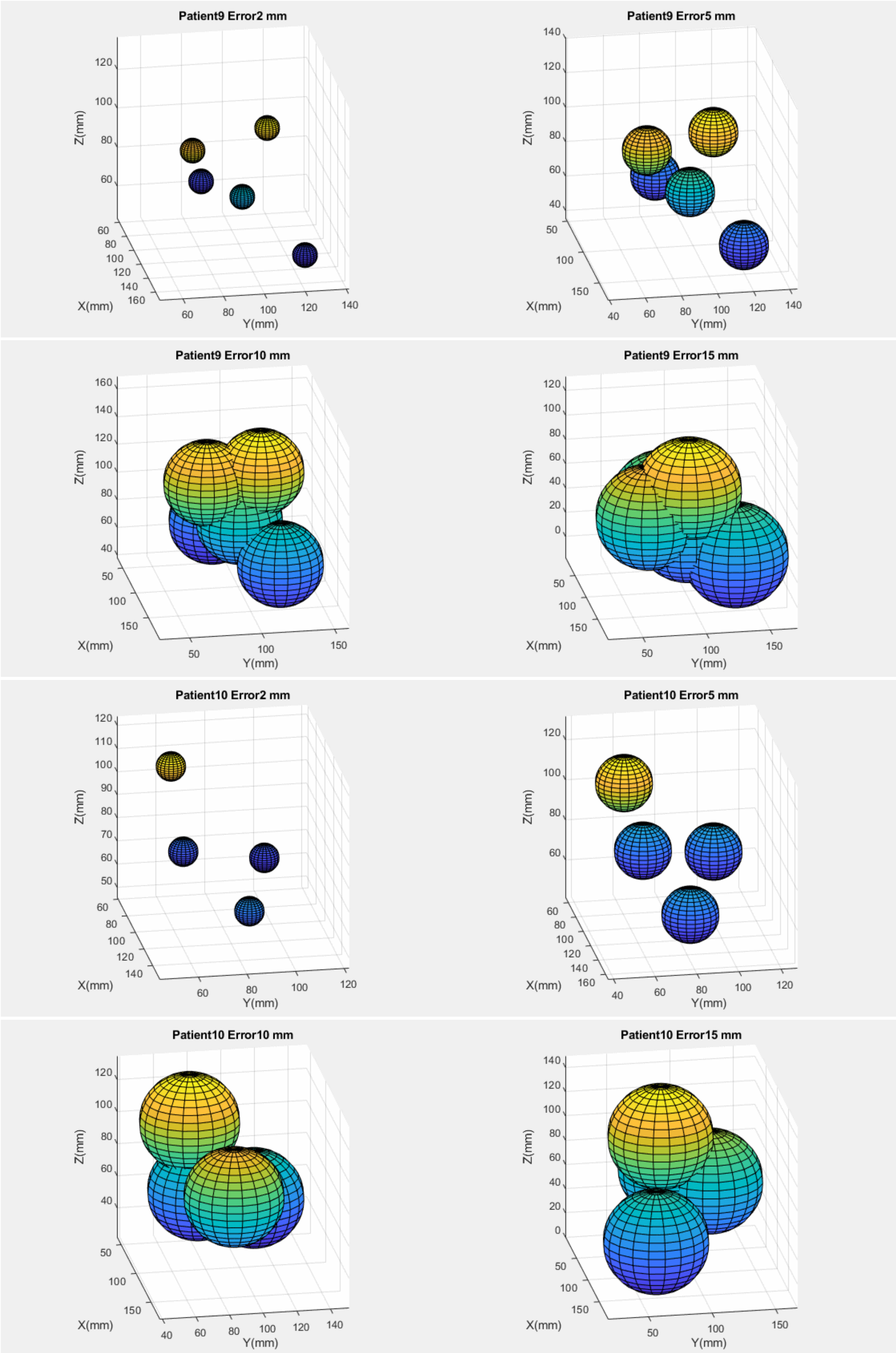
Patient9 Error2 mm
Patient9 Error5 mm
Patient9 Error10 mm
Patient9 Error15 mm
Patient10 Error2 mm
Patient10 Error5 mm
Patient10 Error10 mm
Patient10 Error15 mm
Z(mm)
X(mm)
Y(mm)

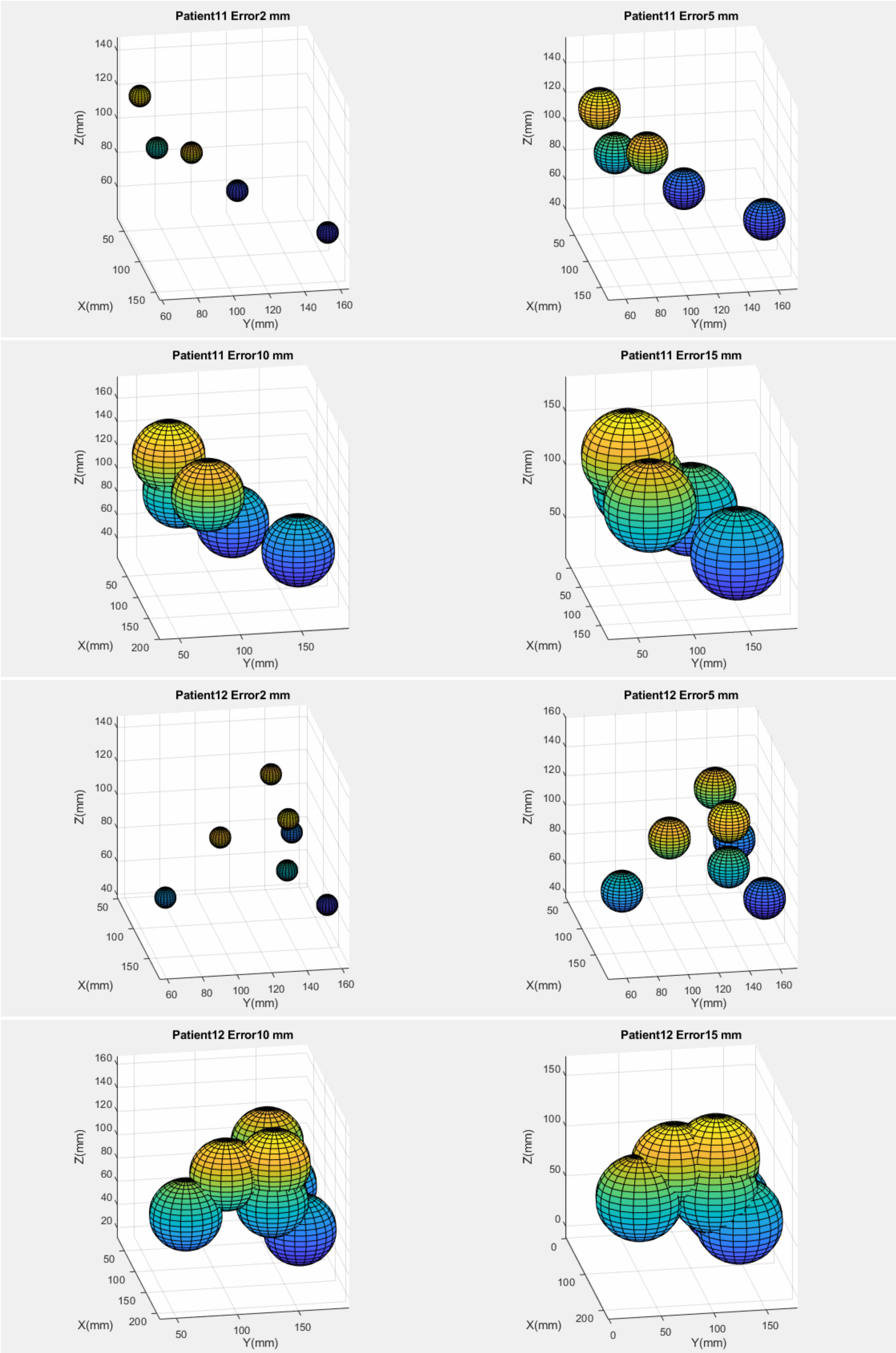
Patient11 Error2 mm
Patient11 Error5 mm
Patient11 Error10 mm
Patient11 Error15 mm
Patient12 Error2 mm
Patient12 Error5 mm
Patient12 Error10 mm
Patient12 Error15 mm
Z(mm)
X(mm)
Y(mm)

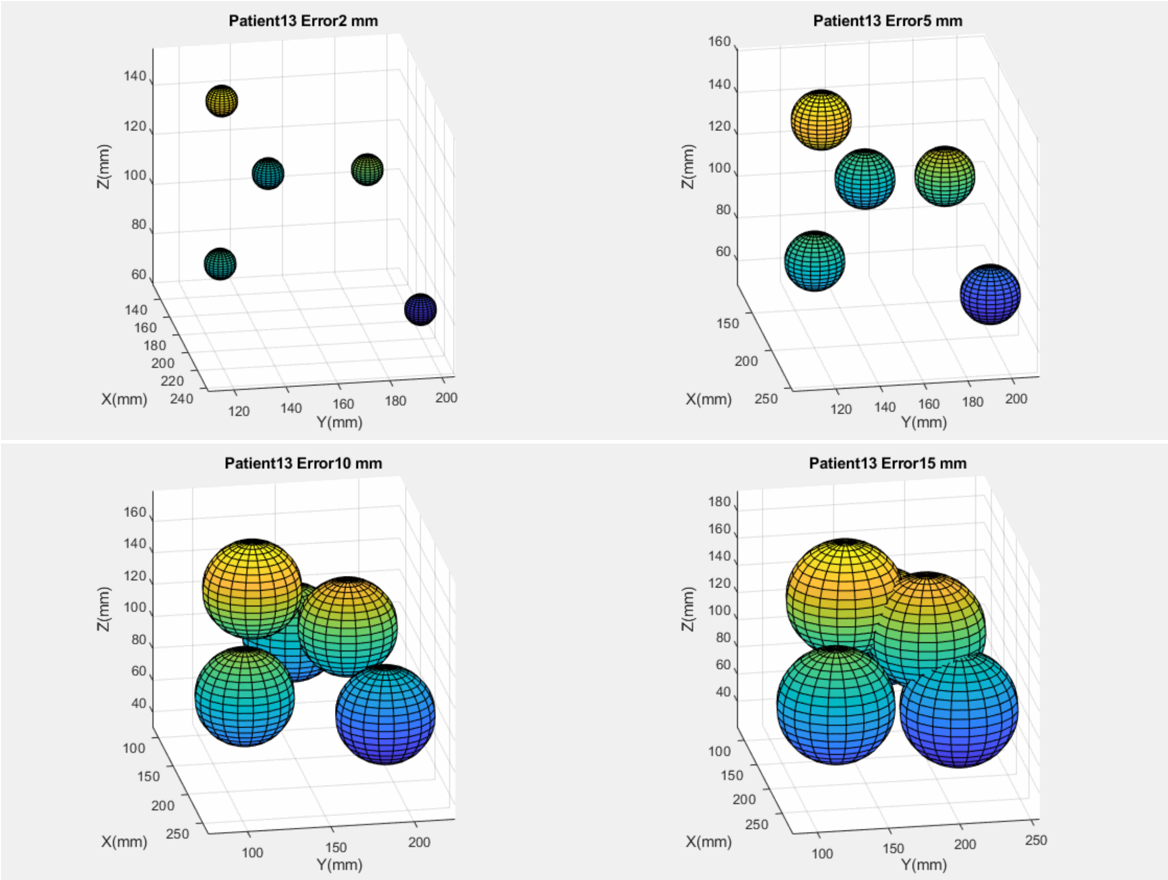
Patient13 Error2 mm
Z(mm)
X(mm)
Y(mm)
Patient13 Error5 mm
Z(mm)
X(mm)
Y(mm)
Patient13 Error10 mm
Z(mm)
X(mm)
Y(mm)
Patient13 Error15 mm
Z(mm)
X(mm)
Y(mm)

Appendix C

Error Group	Avg. rms (mm)	Avg. rms (mm)	p-value	Avg. rms (mm)	p-value	Avg. rms (mm)	p-value
	0 Extra LNs	1 Extra LN	0 vs 1	2 Extra LNs	0 vs 2	3 Extra LNs	0 vs 3
	ICP						
1	2.7±0.6	2.6±0.6	0.4254	2.7±0.7	0.7122	3.9±5.4	0.4190
2	5.8±1.5	6.2±2.0	0.5387	7.5±3.1	0.0703	7.3±2.7	0.1040
3	15.8±8.2	14.8±6.7	0.3786	16.2±7.5	0.8897	16.6±7.9	0.8234
4	22.3±5.2	21.7±11.0	0.8720	22.4±8.2	0.9454	20.6±7.4	0.4140
	CPD						
1	2.6±0.7	2.4±0.7	0.3880	2.4±1.0	0.4511	2.7±1.7	0.8750
2	7.0±2.4	7.9±3.0	0.2587	8.8±3.9	0.1356	8.6±2.6	0.0901
3	16.5±5.1	17.0±5.1	0.7027	19.1±7.6	0.2753	17.6±6.6	0.5905
4	25.2±4.9	27.6±15.1	0. 6324	28.6±13.5	0. 4121	27.9±7.4	0.2927
	Chamfer						
1	2.6±0.6	2.4±0.7	0.3432	2.5±0.9	0.4363	2.7±1.8	0.9023
2	5.8±1.5	6.2±2.0	0.5323	6.7±1.7	0.1437	7.1±1.8	0.0594
3	13.1±4.9	13.6±4.2	0.8096	15.6±8.3	0.3690	14.7±5.6	0.4544
4	24.9±9.3	25.3±19.4	0.9410	24.1±10.6	0.8110	23.8±8.7	0.6639

Table 7. *The average distance between the corresponding LN in the preoperative and intraoperative volume after registration using the three algorithms. The average rms of the distance from preoperative to corresponding intraoperative SN location after the registration from 13 patient SPECT scans is reported, resulting in N=13 pairs per average. The average distance is reported per error distribution and per extra SN. The p-value using the paired t-test (with α=0.0167 after Bonferroni correction) is reported using the 0 extra SNs as baseline.*